Chemical Engineering Journal 470 (2023) 144370

Contents lists available at ScienceDirect

Chemical Engineering Journal

journal homepage: www.elsevier.com/locate/cej

Heterojunction Mo-based binary and ternary nitride catalysts with Pt-like activity for the hydrogen evolution reaction

Xueling Wang [a], Xuming Zhang [a,*], Yifan Xu [a], Hao Song [a], Xingrui Min [a], Zihuan Tang [a], Chaoran Pi [a], Jianping Li [a], Biao Gao [a], Yang Zheng [a], Xiang Peng [c], Paul K. Chu [d], Kaifu Huo [b,*]

[a] The State Key Laboratory of Refractories and Metallurgy, Institute of Advanced Materials and Nanotechnology, Wuhan University of Science and Technology, Wuhan 430081, China

[b] Wuhan National Laboratory for Optoelectronics (WNLO), School of Optical and Electronic Information, Huazhong University of Science and Technology Wuhan 430074, China

[c] Hubei Key Laboratory of Plasma Chemistry and Advanced Materials, Hubei Engineering Technology Research Center of Optoelectronic and New Energy Materials, Wuhan Institute of Technology, Wuhan 430205, China

[d] Department of Physics, Department of Materials Science and Engineering, and Department of Biomedical Engineering, City University of Hong Kong, Tat Chee Avenue, Kowloon, Hong Kong, China

ARTICLE INFO

Keywords:
Ion intercalation
$Mo_2N/Ni_{0.2}Mo_{0.8}N$ heterojunction
Hydrogen evolution reaction
Pt-like activity

ABSTRACT

The development of earth-abundant electrocatalysts with Pt-like catalytic activity for the hydrogen evolution reaction (HER) is of great significance to green hydrogen production. Herein, a novel strategy is described to construct dual-phase nitride nanobelts composed of Mo_2N and $Ni_{0.2}Mo_{0.8}N$ by nitridation of Ni^{2+} intercalated layered MoO_3 nanobelts (NBs). The $Mo_2N/Ni_{0.2}Mo_{0.8}N$ catalyst exhibits superior stability and a low overpotential of 26 mV at 10 mA cm^{-2} and Tafel slope of 31 mV dec^{-1} in both the alkaline electrolyte and simulated seawater, which is comparable to or better than that of the benchmark Pt/C catalyst. The excellent alkaline HER characteristics is attributed to the $Mo_2N/Ni_{0.2}Mo_{0.8}N$ heterostructure with adjustable content and robust interfaces and without metal Ni segregation and structure collapse during nitridation. Density-functional theory (DFT) calculations and experiments reveal that the $Mo_2N/Ni_{0.2}Mo_{0.8}N$ interface with strong electronic interactions optimizes H adsorption/desorption yielding moderately weak bonding metal sites with positive ΔG_{H^*} as the catalytic centers, thereby accelerating the HER kinetics and boosting the HER activity. The results reveal a simple strategy for the preparation of heterostructured nitride-based catalysts with Pt-like activity for hydrogen evolution.

1. Introduction

Hydrogen is one of the promising energy carriers because of its high energy density and zero carbon emission [1–4]. Although water electrolysis is a mature technique for hydrogen production, the efficiency relies on efficient electrocatalysts. Noble metal catalysts represented by Pt/C have shown the best catalytic activity in acidic media so far due to the modest Gibbs free energy of hydrogen adsorption and desorption (ΔG_{H^*}) [5–7], but the alkaline HER kinetics is sluggish as a result of the high energy barrier in water cracking [8,9]. From the perspective of economics and equipment safety, it is urgent to develop low-cost and highly efficient non-noble metal catalysts for the alkaline hydrogen evolution reaction (HER) [10–12], and compounds such as nitrides (TMNs) [13–15], phosphides (TMPs) [16–19], carbides (TMCs) [20–22], and disulfides (TMDs) [23–26] have been investigated as potential candidates.

TMNs are promising alternatives to noble metal-based catalysts because of the Pt-like electronic structure, high electrical conductivity, and excellent corrosion resistance [27,28]. However, the activity of single-phase binary TMNs is worse than that of noble metals because of the improper balance between the water splitting and hydrogen adsorption/desorption activity [29]. For example, the HER activity of Mo_2N is limited by the sluggish desorption of H* due to strong Mo-H* bonding [30,31]. Therefore, it is important to construct nitride-based compounds with the suitable H* adsorption energy in order to enhance the HER kinetics. According to the Brewer-Engel theory, 3*d*

* Corresponding authors.
E-mail addresses: xumzhang@wust.edu.cn (X. Zhang), kfhuo@hust.edu.cn (K. Huo).

https://doi.org/10.1016/j.cej.2023.144370
Received 23 April 2023; Received in revised form 14 June 2023; Accepted 23 June 2023
Available online 24 June 2023

transition metals (Fe, Co, Ni, etc.) have paired electrons in the *d* orbitals and relatively low metal-H* bonding strength [32,33]. Liu et al. have reported a Mo_2N/Ni heterojunction catalyst with excellent HER properties in the alkaline medium [34] and Lang et al. have synthesized nanocomposites of metallic Co and Mo_2N on nitrogen-doped carbon with attractive alkaline HER characteristics [35]. However, the low oxidation resistance and high solubility of pure metal catalysts are problematic in alkaline or chloride-containing electrolytes [36].

Introducing transition metals (Fe, Co, Ni, etc.) into a nitride lattice to from ternary TMNs is a promising strategy to not only enhance the stability by avoiding direct exposure of the metal phase, but also regulate the valence state of Mo sites giving rise to high catalytic activity in hydrogen desorption [37]. Sasaki et al. have observed that non-noble metal nickel-molybdenum nitride possesses the suitable H* adsorption characteristics and excellent acidic HER properties [38]. Liu et al. have studied the HER properties of Ni_xMo_yN by regulating the ratio of Mo and Ni in the precursor and found that $Ni_{0.2}Mo_{0.8}N$ has the best catalytic activity in alkaline HER [39]. Up to now, the alkaline HER activity of these reported ternary TMNs are still inferior to the Pt-based catalysts [40]. Recently, some dual-phase nitrides such as heterostructured $Ni_{0.2}Mo_{0.8}N$/NiN and Mo_2N-Co_xN have been demonstrated and show enhanced HER performance through interfacial modulation to synergistically promoting the water dissociation kinetics and optimizing the hydrogen adsorption/desorption free energy [41,42]. However, the fabrication of nitride-based heterostructures has seldom been reported and their HER mechanism relative to multiple active sites is still obscure [43]. Synthesis of nitride-based composites is usually by one-step nitridation using the corresponding ternary oxide precursor composed of 3*d* and 4*d* transition metal in NH_3 at a high temperature, but the structure are easily collapsed during phase conversion from oxide to nitride and the reaction kinetics of different nitrides are difficult to control at same time under same thermal condition. Secondly, the mass ratio of these formed nitrides and the number of corresponding interfaces is hard to adjust because of the fixed stoichiometric ratio in oxide precursor. Furthermore, these 3*d* transition metal nitrides are not stable and easily transform to metal phase at a high temperature because of the poor thermal stability of interstitial nitrogen atoms. Consequently, controllable synthesis of metal phase free nitride-based heterostructured electrocatalysts is still challenging.

Herein, a dual-phase heterostructured $Mo_2N/Ni_{0.2}Mo_{0.8}N$ nanobelts with robust interfaces are prepared by nitridation of Ni^{2+} intercalated MoO_3 nanobelts. The Ni concentration in the precursor can be tailored to controllably insert Ni^{2+} into the Mo_xN matrix without segregation of the Ni metal phase and structural collapse, and construct a large number of $Mo_2N/Ni_{0.2}Mo_{0.8}N$ interfaces. Furthermore, the in-situ phase conversion successfully form robust interfaces with strong electronic coupling. Therefore, the $Mo_2N/Ni_{0.2}Mo_{0.8}N$ catalyst has superior stability and excellent HER activity manifested by overpotentials of 26 and 127 mV at 10 and 100 mA cm^{-2} in addition to a Tafel slop of 31 mV dec^{-1} in both alkaline and simulated seawater, which are comparable to or better than those of the commercial Pt/C catalyst. Density-functional theory (DFT) calculations demonstrate that the $Mo_2N/Ni_{0.2}Mo_{0.8}N$ interface with strong electronic interactions optimizes H adsorption/desorption yielding moderately weak bonding metal sites with positive ΔG_{H^*} as the catalytic centers in HER. The results demonstrate a novel strategy to design and construct heterostructured nitride-based catalysts for highly efficient water electrolysis.

2. Experimental section

2.1. Materials

The molybdenum metal powder (Mo, reagent grade 99%) and nickel (II) acetate tetrahydrate ($Ni(CH_3COO)_2{\cdot}4H_2O$, labeled as $Ni(Ac)_2$) are purchased from Shanghai Aladdin Biochemical Technology Co., Ltd. Hydrogen peroxide (H_2O_2, 30 wt%) was bought from Sinopharm Chemical Reagent Co., Ltd. (Shanghai, China) and Ni foam (NF) was obtained from Jinghong New Energy Technology Co., Ltd. (Zhengzhou, China). All the chemicals were analytical grade and used without further purification.

2.2. Preparation of MoO_3 nanobelts

The MoO_3 nanobelts were synthesized by a typical hydrothermal method. 1.2 g of the molybdenum metal powder and 6 mL of deionized water (DI Water) were placed in a 250 mL beaker to which 10 mL of hydrogen peroxide (30%) were added under stirring in the ice water bath. After the molybdenum metal powder dissolved, the transparent solution became yellow and 110 mL of DI Water was added to the beaker. After stirring, the solution was transferred and sealed in a 200 mL Teflon-lined stainless-steel autoclave and heated to 180 °C for 24 h in an oven. After the reaction, the MoO_3 nanobelts powder was washed with DI Water and dried at 60 °C for 12 h.

2.3. Preparation of Ni-MoO_3 nanobelts

200 mg of MoO_3, different amounts of $Ni(Ac)_2$ (the molar ratios of nickel to molybdenum are 0.3, 0.4 , 0.5 and 1.0), and 30 mL of anhydrous ethanol were sonicated in a 100 mL beaker, transferred to a 50 mL Teflon-lined stainless-steel autoclave, sealed, and solvothermally treated at 90 °C for 5 h. After the reaction, the Ni^{2+} intercalated MoO_3 nanobelts powder was washed with anhydrous ethanol and dried at 60 °C for 12 h. The samples were designated Ni-MoO_3 (X), X = 0.3, 0.4, 0.5 and 1.0.

2.4. Preparation of $Mo_2N/Ni_{0.2}Mo_{0.8}N$ nanobelts

The Ni^{2+} intercalated MoO_3 powder was placed in a corundum crucible (60 × 30 × 20 mm) and annealed at 600 °C for 3 h in NH_3/Ar to obtain $Mo_2N/Ni_{0.2}Mo_{0.8}N$. According to the pristine ratio of Ni to Mo (X = 0.3, 0.4, and 0.5), the products were labeled as $Mo_2N/Ni_{0.2}Mo_{0.8}N$-1, $Mo_2N/Ni_{0.2}Mo_{0.8}N$-2 and $Mo_2N/Ni_{0.2}Mo_{0.8}N$-3, respectively. As a comparison, the Mo_2N nanobelts was directly formed by annealing the MoO_3 nanobelts in NH_3/Ar at 700 °C for 2 h. The bare $Ni_{0.2}Mo_{0.8}N$ nanobelts was fabricated by annealing the Ni-MoO_3 (1.0) sample in NH_3/Ar at 600 °C for 5 h and subsequent acid pickling in 0.05 M HCl for 6 h at room temperature.

2.5. Preparation of working electrode

First, to eliminate contaminants from the surface of the Cu foam, a small pieces of Cu form with 1 × 1.3 cm^2 was annealed at 750 °C for 10 min in Ar/H_2 ambient. After that, 10 mL of Nafion solution, 1 mL of isopropanol, and 5 mg of catalyst were mixed in a centrifuge tube to form slurry. The slurry was pasted onto a piece of clean Cu foam with active area of 1 cm^2 and dried in a vacuum oven at 70 °C for overnight. For comparison, 20% Pt/C with same loading mass was pasted on Cu foam by same procedure.

2.6. Characterization

The X-ray diffraction (XRD) patterns were acquired in the range of 10° to 90° at a scanning rate of 10° min^{-1} on the Smart-lab diffractometer (Nippon Neo Electric Co., Ltd.) with Cu K_α radiation (λ = 1.54178 Å). The scanning electron microscopy (SEM) images were taken on the Apreo S HiVac field-emission scanning electron microscopy (Seamer Fisher technology co., Ltd.) and transmission electron microscopy (TEM), high-angle annular dark-field scanning TEM (HAADF-STEM), and energy-dispersive X-ray spectroscopy (EDS) were performed on the JEM-F200X transmission electron microscopy (Japan Electronics Co., Ltd.) equipped with an energy dispersive X-ray detector. The X-ray photoelectron spectra (XPS) were obtained on the AXIS SUPRA+ X-ray

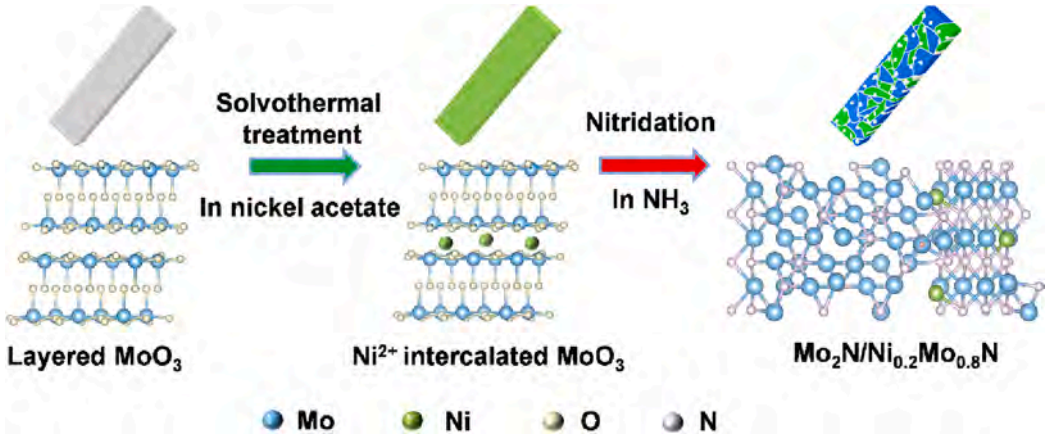

Fig. 1. Schematic illustration of the synthesis of dual phase $Mo_2N/Ni_{0.2}Mo_{0.8}N$ NBs.

photoelectron spectrometer (Shimadzu testing Technology Co., Ltd.) and the Mo and Ni concentrations in the samples were determined by inductively-coupled plasma mass spectrometry (ICP-MS) on the NexION 1000G.

2.7. Electrochemical measurements

The electrochemical measurements were carried out on the Biologic Science Instruments VSP30 electrochemical workstation. The catalytic hydrogen evolution properties were determined using a three-electrode system and the overall water splitting characteristics were evaluated based on a two-electrode system. The saturated calomel electrode (SCE) and carbon rod were the reference and counter electrodes, respectively. The prepared catalysts or Pt/C powder with the same mass loading of 5 mg were coated on the copper foam as the working electrode and the electrolyte was 1.0 M KOH. The polarization curves were calibrated to the reversible hydrogen electrode (RHE) by $E_{(RHE)} = E_{(SCE)} + 0.2415$ V $+ 0.0592 \times$ pH with *iR* compensation and the current densities (*j*) were normalized by the geometric surface area. The electrode was activated by cyclic voltammetry (CV) in Faraday interval (−33 to −133 mV vs. RHE) to reach a stable state and then the polarization curves were obtained by linear sweep voltammetry (LSV) at a scanning rate of 5 mV s^{-1}. Cyclic voltammetry (CV) was conducted at different sweep rates (10, 20, 30, 40 and 50 mV s^{-1}) in the non-Faraday interval (−0.85 V ~ −0.95 V

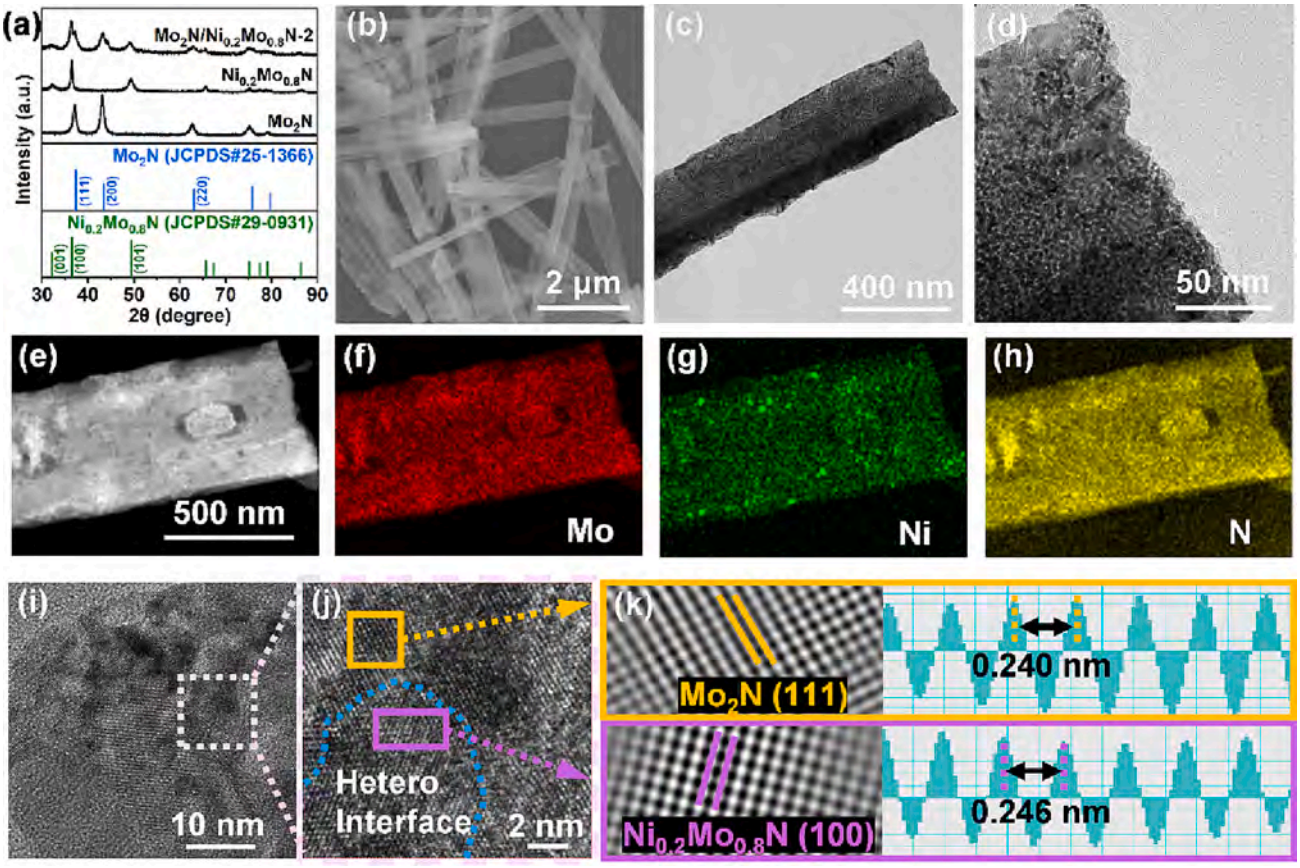

Fig. 2. (a) XRD patterns of Mo_2N, $Ni_{0.2}Mo_{0.8}N$, and $Mo_2N/Ni_{0.2}Mo_{0.8}N$-2; (b-d) SEM and TEM images of $Mo_2N/Ni_{0.2}Mo_{0.8}N$-2; (e-h) STEM image and EDS elemental maps of Mo, Ni, and N of $Mo_2N/Ni_{0.2}Mo_{0.8}N$-2; (i-j) HR-TEM images of $Mo_2N/Ni_{0.2}Mo_{0.8}N$-2; (k) Inverse FFT lattice images and interplanar spacing profiles.

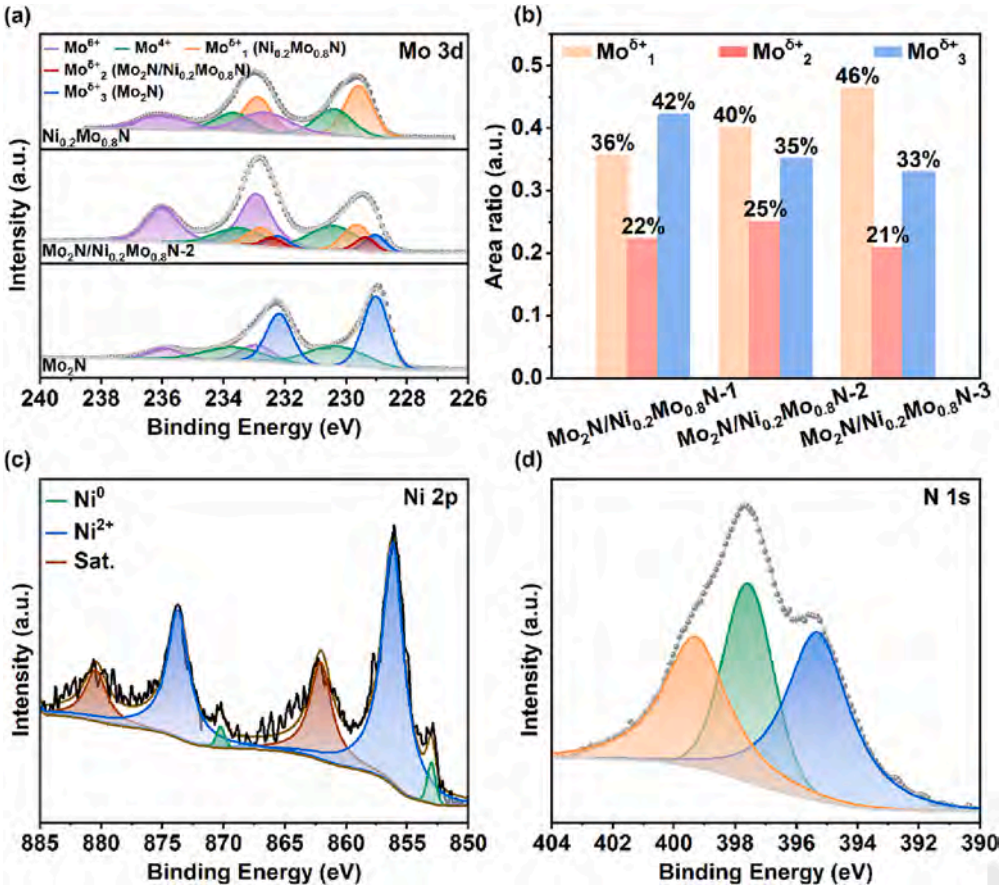

Fig. 3. High-resolution XPS spectra of (a) Mo 3*d* of, $Ni_{0.2}Mo_{0.8}N$, Mo_2N, and $Mo_2N/Ni_{0.2}Mo_{0.8}N$-2; (c) Ni 2*p*; (d) N 1*s* of $Mo_2N/Ni_{0.2}Mo_{0.8}N$-2; (b) the area ratio of different Mo valence states symbolizing different nitrides in $Mo_2N/Ni_{0.2}Mo_{0.8}N$.

(vs. SCE)). The difference between the forward and reverse currents in the CV curves reflected the magnitude of the double layer capacitances (C_{dl}). The ECSAs were calculated from the double-layer capacitance by the equation: ECSA = C_{dl}/60 μF cm^{-2} [44]. The stability was assessed by chronoamperometry at a constant overpotential.

2.8. Computation

The Vienna Ab Initio Package (VASP) [45,46] was employed to perform the density-functional theory (DFT) calculation within the generalized gradient approximation (GGA) using the PBE formulation [47]. The projected augmented wave (PAW) potentials [48,49] were chosen to describe the ionic cores and take valence electrons into account using a plane wave basis set with a kinetic energy cutoff of 400 eV. Partial occupancies of the Kohn − Sham orbitals were allowed using the Gaussian smearing method and a width of 0.05 eV. The electronic energy was considered self-consistent when the energy change was smaller than 10^{-5} eV and the geometric optimization was considered convergent when the force change was smaller than 0.02 eV/Å. The Grimme's DFT-D3 methodology was utilized to describe the dispersion interactions [50].

3. Results and discussion

3.1. Preparation and characterization of $Mo_2N/Ni_{0.2}Mo_{0.8}N$

The synthesis of the heterostructured $Mo_2N/Ni_{0.2}Mo_{0.8}N$ catalyst is illustrated schematically in Fig. 1. The layered MoO_3 NBs prepared hydrothermally are immersed in a nickel acetate solution at 90 °C for 6 h to produce the Ni inserted MoO_3 nanobelts (Ni-MoO_3) [51]. The XRD peaks of the hydrothermal powder are in good agreement with those of MoO_3 (JCPDS#05-0850). The peak of the (0 2 0) plane at 12.5° shows an apparent shift to a smaller angle after immersion, suggesting an enlarged interlayer spacing stemming from insertion of Ni^{2+} (Fig. S1a) [52]. Inductively-coupled plasma mass spectrometry (ICP-MS) is performed to calculate the Ni concentration in the Ni-MoO_3 composites with increasing feeding molar ratios of Ni to Mo from 0.3 to 0.5 (Fig. S1b). The molar ratios of Ni to Mo in Ni-MoO_3 changes from 0.18 to 0.31, showing a positive correlation towards to the feeding molar ratios. However, when the molar ratio of Ni to Mo is 0.5, a peak at 11.5° emerges from $Ni(OH)_2{\cdot}0.75H_2O$ (JCPDS#38-0715) due to self-deposition of Ni^{2+} on the surface at the high concentration. The color of the MoO_3 NBs powder changes from white to light green after immersion and then to black after nitridation at 600 °C for 3 h (Fig. S2). Fig. 2a shows two sets of XRD patterns with diffraction peaks at 37.4°, 43.5°, 63.1°, and 75.7° as well as 32.2°, 36.5°, and 49.4° corresponding to cubic Mo_2N (JCPDS#25-1366) [53] and hexagonal $Ni_{0.2}Mo_{0.8}N$ (JCPDS#29-0931) [54], respectively, from the nitrided sample of Ni-MoO_3 (0.4) (labeled as $Mo_2N/Ni_{0.2}Mo_{0.8}N$-2). The relative mass ratios of Mo_2N to $Ni_{0.2}Mo_{0.8}N$ decrease based on the Rietveld refinement analysis, suggesting conversion of more Mo_2N to $Ni_{0.2}Mo_{0.8}N$ with increasing Ni concentrations in the Ni-MoO_3 composites (Fig. S3). However, the crystalline cubic Ni phase (JCPDS#04-0850) showing peaks at 44.5°, 51.8° and 76.4° are observed from $Mo_2N/Ni_{0.2}Mo_{0.8}N$-3 after nitridation due to reduction of surface $Ni(OH)_2{\cdot}0.75H_2O$ (JCPDS#38-0715).

The scanning electron microscopy (SEM) images of MoO_3, Ni-MoO_3 (0.3), Ni-MoO_3 (0.4), and Ni-MoO_3 (0.5) are displayed in Fig. S4. The pristine MoO_3 NBs have a width of approximately 300 nm. After Ni^{2+} insertion and nitridation, $Mo_2N/Ni_{0.2}Mo_{0.8}N$-1 and $Mo_2N/Ni_{0.2}Mo_{0.8}N$-

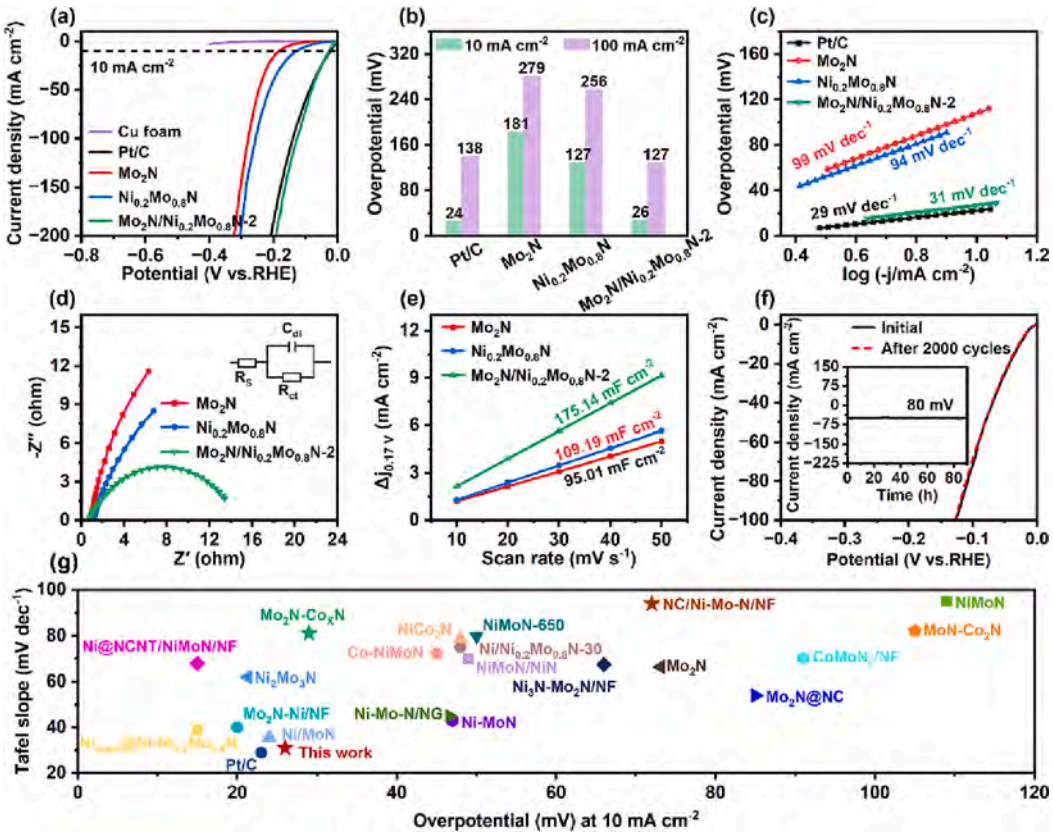

Fig. 4. (a) LSV curves; (b) Overpotentials at current densities of 10 mA cm^{-2} and 100 mA cm^{-2}; (c) Tafel slopes; (d) Nyquist plots; (e) Double-layer capacitance (C_{dl}); (f) Polarization curves before and after 2,000 CV cycles in Faraday interval (−33 to −133 mV vs. RHE) (inset showing the chronoamperometric test of Mo_2N/$Ni_{0.2}Mo_{0.8}N$-2 at a constant overpotential of 80 mV for 90 h); (g) Comparison of η_{10} and Tafel slope values of Mo_2N/$Ni_{0.2}Mo_{0.8}N$-2 and those of other reference catalysts in 1.0 M KOH.

2 retain the smooth nanobelt morphology (Fig. S5a and Fig. 2b-c). However, some nanoparticles are uniformly dispersed on the surface of Mo_2N/$Ni_{0.2}Mo_{0.8}N$-3 because of surface reduction of $Ni(OH)_2{\cdot}0.75H_2O$ to metallic Ni (Fig. S5b). To further study the distributions of the Ni species and microstructure after nitridation, Mo_2N/$Ni_{0.2}Mo_{0.8}N$-2 is examined by HR-TEM, as shown in Fig. 2d, which discloses a large number of uniformly distributed mesopores with 5–10 nm in size in the NBs. The porosity features of Mo_2N/$Ni_{0.2}Mo_{0.8}N$-2 is further evaluated by N_2 adsorption and desorption measurements using the Barrett–Joyner–Halenda (BJH) method (Fig. S6). The Mo_2N/$Ni_{0.2}Mo_{0.8}N$-2 exhibits a typical mesoporous characteristic with a type-IV isotherm, showing a high specific surface area of 80.53 $m^2\ g^{-1}$, which is larger than that of MoO_3 (50.41 $m^2\ g^{-1}$) and Mo_2N NBs (54.97 $m^2\ g^{-1}$). The pore-size distribution of Mo_2N/$Ni_{0.2}Mo_{0.8}N$-2 demonstrates the average pore-sizes of about 7.7 nm, in line with the TEM result. The EDS elemental maps in Fig. 2e-h confirm that Mo, Ni, and N are uniformly distributed with the exception of a few aggregates of Ni species resulting from reduction of residual surface nickel hydroxide. The high-resolution TEM (HR-TEM) images in Fig. 2i-k disclose visible interfaces and lattice fringes with spacings of 0.246 and 0.208 nm corresponding to the (1 0 0) plane of $Ni_{0.2}Mo_{0.8}N$ and (1 1 1) plane of Mo_2N, respectively. These results corroborate successful fabrication of the heterostructured Mo_2N/$Ni_{0.2}Mo_{0.8}N$ NBs with tailored compositions and abundant mesopores by cationic intercalation and nitridation.

X-ray photoelectron spectroscopy (XPS) is performed to determine the chemical states of Mo_2N/$Ni_{0.2}Mo_{0.8}N$ NBs. Fig. 3a shows the high-resolution Mo 3*d* spectra of Mo_2N, $Ni_{0.2}Mo_{0.8}N$ and Mo_2N/$Ni_{0.2}Mo_{0.8}N$-2. There are two fitted double peaks at 229.64/232.78 eV and 229.04/232.22 eV ascribed to $Mo_1^{\delta+}$ and $Mo_3^{\delta+}$ in $Ni_{0.2}Mo_{0.8}N$ and Mo_2N, respectively [55–57]. An additional pair of fitted peaks at 229.37 and 232.42 eV can be assigned to $Mo_2^{\delta+}$ from $Ni_{0.2}Mo_{0.8}N$ and Mo_2N interface [58–60]. The other fitted doublet peaks at 230.43/233.48 eV and 232.90/235.95 eV are related to Mo^{4+} (MoO_2) and Mo^{6+} (MoO_3) arising from surface oxidation of the nitride. The area ratio of interfacial $Mo_2^{\delta+}$ to whole $Mo^{\delta+}$ in Mo_2N/$Ni_{0.2}Mo_{0.8}N$-2 is 25.1 % (Fig. 3b), which is bigger than those of Mo_2N/$Ni_{0.2}Mo_{0.8}N$-1 (22%) and Mo_2N/$Ni_{0.2}Mo_{0.8}N$-3 (21%), revealing a large amount of heterointerfaces in Mo_2N/$Ni_{0.2}Mo_{0.8}N$-2. These results indicate that the Mo_2N/$Ni_{0.2}Mo_{0.8}N$ interface is influenced by the mass ratio of Mo_2N to $Ni_{0.2}Mo_{0.8}N$ and the proper mass ratio leads to the formation of more interfaces. The high-resolution Ni 2*p* spectrum of Mo_2N/$Ni_{0.2}Mo_{0.8}N$-2 in Fig. 3c shows three double peaks at 853.03/870.26 eV and 856.18/873.73 eV stemming from some metallic Ni^0 and dominant Ni^{2+} in $Ni_{0.2}Mo_{0.8}N$, respectively, in addition to the satellite peaks of Ni^{2+} at 862.06/880.43 eV. However, the peak of metallic Ni^0 cannot be observed from Mo_2N/$Ni_{0.2}Mo_{0.8}N$-1 and high intensity if Ni^0 is shown from Mo_2N/$Ni_{0.2}Mo_{0.8}N$-3 (Fig. S7) [61]. Similarly, the N 1 *s* spectra exhibits three peaks attributable to metal-N (397.57 eV), N-H (399.30 eV) and Mo 3*d* (395.31 eV) (Fig. 3d).

3.2. Electrochemical measurement

To evaluate the HER characteristics of Mo_2N/$Ni_{0.2}Mo_{0.8}N$ NBs, the polarization curves are performed. The commercial 20 wt% Pt/C, Mo_2N NBs, and $Ni_{0.2}Mo_{0.8}N$ NBs with the same mass loading of 5 mg cm^{-2} are compared. The $Ni_{0.2}Mo_{0.8}N$ NBs was obtained by nitridation of Ni-MoO_3 (1.0) and subsequent acid pickling (Fig. S8). The polarization curves are *iR* corrected automatically. These Mo_2N/$Ni_{0.2}Mo_{0.8}N$ catalyst shows enhanced HER activity than that of bare Mo_2N (181 and 279 mV) and $Ni_{0.2}Mo_{0.8}N$ (127 and 256 mV) (Fig. S9), and the optimal Mo_2N/

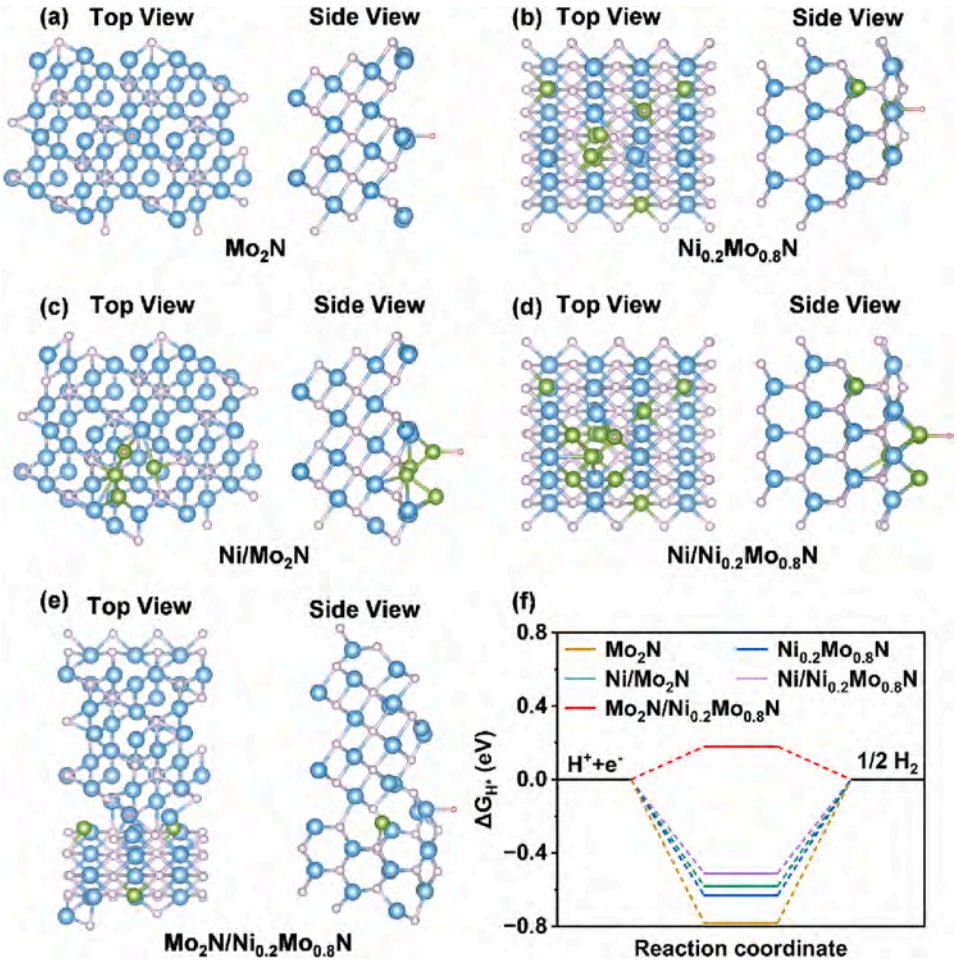

Fig. 5. (a-e) Top and side views of the schematic models of Mo_2N (1 1 1), $Ni_{0.2}Mo_{0.8}N$ (1 0 0), Ni cluster/Mo_2N (1 1 1), Ni cluster/$Ni_{0.2}Mo_{0.8}N$ (1 0 0), and Mo_2N (1 1 1)/$Ni_{0.2}Mo_{0.8}N$ (1 0 0); (f) Free energy diagram of HER at the equilibrium potential.

$Ni_{0.2}Mo_{0.8}N$-2 catalyst shows the best HER characteristics with small overpotentials of 26 and 127 mV at current densities of 10 and 100 mA cm^{-2} and the performance is close to that of Pt/C (23 and 140 mV) (Fig. 4a-b). The Tafel slope of $Mo_2N/Ni_{0.2}Mo_{0.8}N$-2 is only about 31 mV dec^{-1}, which is also similar to that of ideal Pt/C (29 mV dec^{-1}) and much smaller than those of Mo_2N (99 mV dec^{-1}) and $Ni_{0.2}Mo_{0.8}N$ (94 mV dec^{-1}) (Fig. 4c). The reaction kinetics suggests the favorable Volmer-Tafel HER mechanism for $Mo_2N/Ni_{0.2}Mo_{0.8}N$-2 and the Tafel step is the rate determining step (RDS) [62]. The heterogeneous interface between Mo_2N and $Ni_{0.2}Mo_{0.8}N$ is the dominant active center. The charge transfer resistance (R_{ct}) of $Mo_2N/Ni_{0.2}Mo_{0.8}N$-2 dramatically decreases in comparison with the bare $Ni_{0.2}Mo_{0.8}N$ and Mo_2N (Fig. 4d). It has been reported that the interface between metallic Ni and Mo_2N or $Ni_{0.2}Mo_{0.8}N$ affects adsorption of reactants and/or intermediates consequently modulating the HER activity [63–65]. The HER activity of $Mo_2N/Ni_{0.2}Mo_{0.8}N$-2 is investigated before and after removing surface metallic Ni in 0.05 M HCl for 3 h at room temperature. After removal, the metallic Ni phase disappears but the $Ni_{0.2}Mo_{0.8}N$ and Mo_2N phases are not changed (Fig. S10). The overpotentials of acid pickled $Mo_2N/Ni_{0.2}Mo_{0.8}N$-2 show slight decay of 6 mV and 18 mV at current density of 10 and 100 mA cm^{-2}, but it is better than that of metal phase free $Mo_2N/Ni_{0.2}Mo_{0.8}N$-1 sample, further suggesting that the decorated Ni metal phase on surface is not the dominated factor for the HER activity, but which can accelerate surface electron transport (Fig. S11). The turnover frequency (TOF) of $Mo_2N/Ni_{0.2}Mo_{0.8}N$-2 is calculated to be 0.19 s^{-1} at an overpotential of 200 mV, which is much higher than those of $Ni_{0.2}Mo_{0.8}N$ (0.07 s^{-1}) and Mo_2N (0.06 s^{-1}), further corroborating the high intrinsic catalytic activity of $Mo_2N/Ni_{0.2}Mo_{0.8}N$-2 (Fig. S12). The faradic efficiency of $Mo_2N/Ni_{0.2}Mo_{0.8}N$-2 catalyst during HER catalytic process is assessed in a three-electrode system under different applied current for 30 min and about 99% FE is obtained (Fig. S13).

The electrochemical surface area (ECSA) reflected by the electrochemical double layer capacitance (C_{dl}) can be derived from the CV curves in the non-Faraday range (Fig. S14). As shown in Fig. 4e, C_{dl} value of $Mo_2N/Ni_{0.2}Mo_{0.8}N$-2 is 175.14 mF cm^{-2} which is about 1.7 times larger than that of $Ni_{0.2}Mo_{0.8}N$ (109.19 mF cm^{-2}), almost 2 times larger than that of Mo_2N (95.01 mF cm^{-2}). The larger C_{dl} reflects more exposed active sites on $Mo_2N/Ni_{0.2}Mo_{0.8}N$-2 due to abundant mesopores and interfaces. The electrochemical stability is assessed and shown in Fig. 4f. After 2,000 CV cycles at a scanning rate of 50 mV s^{-1} in Faraday interval (−33 to −133 mV vs. RHE) and chronoamperometric test at a constant overpotential of 80 mV for 90 h, almost no deterioration is observed, consequently corroborating the superior HER stability of $Mo_2N/Ni_{0.2}Mo_{0.8}N$-2 in 1.0 M KOH. After the duration test, $Mo_2N/Ni_{0.2}Mo_{0.8}N$-2 catalyst retains the original nanobelt morphology, mesoporous structure, crystalline and chemical valences of Mo 3*d* and Ni 2*p* (Figs. S15–17), demonstrating the good structure stability. The excellent stability of $Mo_2N/Ni_{0.2}Mo_{0.8}N$ arises from the good corrosion resistance and high conductivity of nitrides. In fact, the $Mo_2N/Ni_{0.2}Mo_{0.8}N$ heterostructures exhibit superior HER activity and kinetics comparable to Pt/C catalyst and even better than those of most recently reported nitride-based catalysts (Fig. 4g and Table S1) in alkaline media.

3.3. Theoretical calculation

To elucidate the mechanism of the HER activity of the $Mo_2N/$

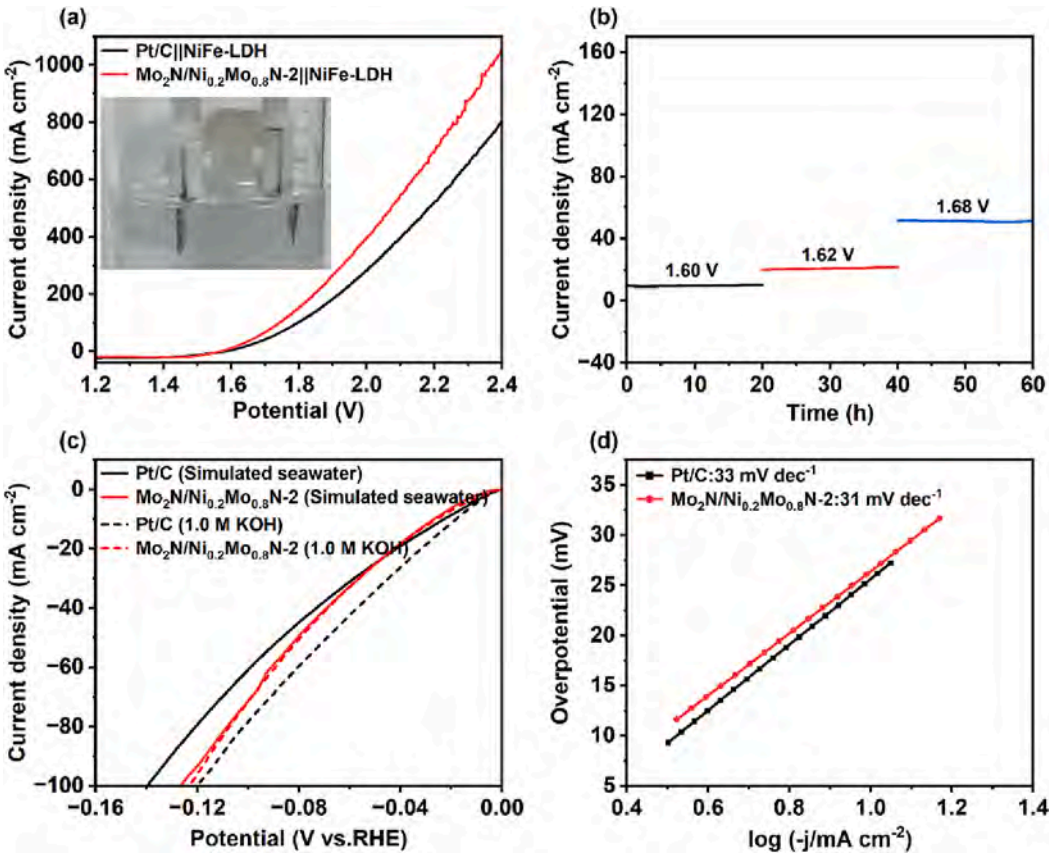

Fig. 6. (a) LSV curves of $Mo_2N/Ni_{0.2}Mo_{0.8}N$-2||NiFe LDH and Pt/C||NiFe LDH in overall water splitting (inset showing the photograph of the two-electrode system); (b) Long-term stability of $Mo_2N/Ni_{0.2}Mo_{0.8}N$-2||NiFe LDH in overall water splitting at various potential in 1.0 M KOH; (c, d) LSV curves and Tafel slopes of $Mo_2N/Ni_{0.2}Mo_{0.8}N$-2 and Pt/C in simulated seawater (1.0 M KOH + 0.5 M NaCl).

$Ni_{0.2}Mo_{0.8}N$ heterojunction, density-functional theory (DFT) calculation is carried out based on the model that couples lattice matched $Ni_{0.2}Mo_{0.8}N$ (100) and Mo_2N (111) according to the XRD and TEM results. It is well known that ΔG_{H^*} is an important parameter to evaluate the activity of catalysts by measuring the Gibbs free energy of hydrogen adsorption/desorption [65–67]. As an important rate determining step, the energy barrier in the Tafel reaction is calculated and Fig. 5 shows the possible heterointerfaces that can affect the HER activity. The bare Mo_2N and $Ni_{0.2}Mo_{0.8}N$ surfaces show more negative ΔG_{H^*} of −0.78 eV and −0.63 eV, respectively, implying restricted hydrogen desorption. After coupling with metallic Ni, the ΔG_{H^*} values of Ni/Mo_2N and Ni/$Ni_{0.2}Mo_{0.8}N$ interfaces are −0.58 eV and −0.51 eV corresponding to the enhanced hydrogen desorption activity. With regard to the Mo_2N/$Ni_{0.2}Mo_{0.8}N$ heterojunction, the interfacial Mo site has ΔG_{H^*} of 0.18 eV when two strongly adsorbing sites on Mo_2N and $Ni_{0.2}Mo_{0.8}N$ are coupled, therefore, desorption of hydrogen possibly occurs on the interfacial Mo site. Sun et al. have proposed that the strongly adsorbing sites with negative ΔG_{H^*} could act as spectators rather than participating in the HER while the weakly bound hydrogens (enabled on sites with the $\Delta G_{H^*} > 0$) drive the HER forward in the multiple adsorption site model [68]. According to the findings, the weakly bound metal sites with $G_{H^*} > 0$ may serve as the actual active site for hydrogen desorption, enhancing HER kinetics.

3.4. Practical application in electrolyzer and simulated seawater

To demonstrate the practicality and commercial potential of Mo_2N/$Ni_{0.2}Mo_{0.8}N$, an electrolyzer is assembled with the cathode of Mo_2N/$Ni_{0.2}Mo_{0.8}N$-2 and anode of NiFe-LDH for overall water splitting in 1.0 M KOH and simulated seawater (1.0 M KOH + 0.5 M NaCl). The OER performance of the NiFe-LDH is described in Fig. S18. Fig. 6a shows that the $Mo_2N/Ni_{0.2}Mo_{0.8}N$-2||NiFe-LDH electrolyzer requires only 1.60 V and 1.74 V to reach current densities of 10 and 100 mA cm^{-2} in the two-electrode system, which are lower than those of Pt/C||NiFe-LDH (1.62 V at 10 mA cm^{-2}, 1.79 V at 100 mA cm^{-2}). The chronoamperometric curve of the water splitting system shows negligible degradation after operation at different voltages for over 60 h (Fig. 6b). To assess Faradic efficiency of overall water splitting of $Mo_2N/Ni_{0.2}Mo_{0.8}N$-2||NiFe-LDH electrolyzer, the H_2 and O_2 gas generated from the cathode and anode electrode at a constant current of 200 mA for 60 min are collected using the drainage method (Fig. S19). The volume ratio of collected H_2 to O_2 gas is 2, and the faradic efficiency of its overall water splitting reaction is about 57.4%. In simulated seawater (Fig. 6c-d), the polarization curve of $Mo_2N/Ni_{0.2}Mo_{0.8}N$-2 shows small overpotentials of 26 and 127 mV at 10 and 100 mA cm^{-2} and the Tafel slope of 31 mV dec^{-1} is the same as that in the alkaline medium. In contrast, Pt/C exhibits visible overpotentials decay from 23 and 140 mV at 10 and 100 mA cm^{-2} in 1.0 M KOH to 28 and 155 mV in simulated seawater and the Tafel slope increases to 33 mV dec^{-1}, suggesting high corrosion resistance to Cl^- ions and applicability of $Mo_2N/Ni_{0.2}Mo_{0.8}N$ [69]. During the test conducted at a constant overpotential of 80 mV for 12 h in simulated seawater, the current shows no decline (Fig. S20). The excellent versatility and efficiency of the $Mo_2N/Ni_{0.2}Mo_{0.8}N$ catalyst for HER applications is thus demonstrated.

4. Conclusion

A dual-phase nitride-based heterostructure composed of Mo_2N and $Ni_{0.2}Mo_{0.8}N$ is prepared by nitridation of Ni^{2+} intercalated layered MoO_3 nanobelts. The Ni^{2+} species inserted in layered MoO_3 avoid

segregation of metal Ni phase and structural damage to form more interfaces. The $Mo_2N/Ni_{0.2}Mo_{0.8}N$ heterostructure with robust interfaces and strong interfacial interactions exhibits superior Pt-like HER activity manifested by an extremely low overpotential of 26 mV at 10 mA cm^{-2} and ideal Tafel slop of 31 mV dec^{-1} in both alkaline and simulated seawater. Moreover, the $Mo_2N/Ni_{0.2}Mo_{0.8}N$ catalyst has excellent practicality and stability in overall water splitting in both the alkaline electrolyte and simulated seawater. Beside the structural advantage, the excellent hydrogen evolution characteristics of dual-phase nitride composite are also attributed to not only the strong water dissociation activity of individual nitride, but also optimization of the hydrogen adsorption/desorption activity at the interfacial sites, especially the weak hydrogen adsorption capability. Herein, our results demonstrate the immense potential of highly electrocatalytically active dual-phase nitride-based catalysts for water splitting and the design and fabrication strategy are suitable for high-performance heterostructured electrocatalysts for efficient energy conversion.

CRediT authorship contribution statement

Xueling Wang: Data curation, Formal analysis, Writing – original draft. **Xuming Zhang:** Conceptualization, Writing – review & editing, Supervision. **Yifan Xu:** Data curation, Investigation. **Hao Song:** Data curation, Investigation. **Xingrui Min:** Data curation, Investigation. **Zihuan Tang:** Data curation, Investigation, Software. **Chaoran Pi:** Data curation, Investigation. **Jianping Li:** Investigation. **Biao Gao:** Resources, Investigation. **Yang Zheng:** Investigation. **Xiang Peng:** Investigation. **Paul K. Chu:** Resources, Writing – review & editing. **Kaifu Huo:** Conceptualization, Resources, Supervision.

Declaration of Competing Interest

The authors declare that they have no known competing financial interests or personal relationships that could have appeared to influence the work reported in this paper.

Data availability

Data will be made available on request.

Acknowledgements

This work was financially supported by National Key R&.D Program of China (2022VFB2404800), National Science Foundation of China, China (Nos. U2004120 and U2003130), Application Foundation Frontier Project of Wuhan Science and Technology Program, Hubei, Chian (2020010601012199), the Basic Research Program of Shenzhen Municipal Science and Technology Innovation Committee (JCYJ20210324141613032), Shenzhen, China, Outstanding Youth Foundation of Natural Science Foundation of Hubei Province, Hubei, China (2020CFA099), Innovation group of Natural Science Foundation of Hubei Province, Hubei, China (2019CFA020), City University of Hong Kong Strategic Research Grant (SRG), Hong Kong, China (7005505), and City University of Hong Kong Donation Research Grant, Hong Kong, China (DON-RMG 9229021).

Appendix A. Supplementary data

Supplementary data to this article can be found online at https://doi.org/10.1016/j.cej.2023.144370.

References

[1] I. Staffell, D. Scamman, A. Velazquez Abad, P. Balcombe, P.E. Dodds, P. Ekins, N. Shah, K.R. Ward, The role of hydrogen and fuel cells in the global energy system, Energy Environ. Sci. 12 (2019) 463–491, https://doi.org/10.1039/c8ee01157e.

[2] M.D. Leonard, E.E. Michaelides, D.N. Michaelides, Energy storage needs for the substitution of fossil fuel power plants with renewables, Renew. Energy. 145 (2020) 951–962, https://doi.org/10.1016/j.renene.2019.06.066.

[3] S.R. Sharvini, Z.Z. Noor, C.S. Chong, L.C. Stringer, R.O. Yusuf, Energy consumption trends and their linkages with renewable energy policies in East and Southeast Asian countries: Challenges and opportunities, Sustain. Environ. Res. 28 (2018) 257–266, https://doi.org/10.1016/j.serj.2018.08.006.

[4] S. Liu, W. Kuang, X. Meng, W. Qi, S. Adimi, H. Guo, X. Guo, E. Pervaiz, Y. Zhu, D. Xue, M. Yang, Dual-phase metal nitrides as highly efficient co-catalysts for photocatalytic hydrogen evolution, Chem. Eng. J. 416 (2021), 129116, https://doi.org/10.1016/j.cej.2021.129116.

[5] F. Li, G.F. Han, H.J. Noh, J.P. Jeon, I. Ahmad, S. Chen, C. Yang, Y. Bu, Z. Fu, Y. Lu, J.B. Baek, Balancing hydrogen adsorption/desorption by orbital modulation for efficient hydrogen evolution catalysis, Nat. Commun. 10 (2019) 1–7, https://doi.org/10.1038/s41467-019-12012-z.

[6] J. Liu, C. Tang, Z. Ke, R. Chen, H. Wang, W. Li, C. Jiang, D. He, G. Wang, X. Xiao, Optimizing hydrogen adsorption by d–d orbital modulation for efficient hydrogen evolution catalysis, Adv. Energy Mater. 12 (2022) 1–9, https://doi.org/10.1002/aenm.202103301.

[7] J. Zhu, S. Mu, Parsing the basic principles to build efficient heterostructures toward electrocatalysis, Inorg. Chem. Front. 10 (2023) 2220–2225, https://doi.org/10.1039/D3QI00117B.

[8] B.A. Yusuf, W. Yaseen, M. Xie, R.S. Zayyan, A.I. Muhammad, R. Nankya, J. Xie, Y. Xu, Recent advances in understanding and design of efficient hydrogen evolution electrocatalysts for water splitting: A comprehensive review, Adv. Colloid Interface Sci. 311 (2023), 102811, https://doi.org/10.1016/j.cis.2022.102811.

[9] J. Zhu, L. Hu, P. Zhao, L.Y.S. Lee, K.-Y. Wong, Recent advances in electrocatalytic hydrogen evolution using nanoparticles, Chem. Rev. 120 (2020) 851–918, https://doi.org/10.1021/acs.chemrev.9b00248.

[10] H. Shen, S. Liang, S. Adimi, X. Guo, Y. Zhu, H. Guo, T. Thomas, J.P. Attfield, M. Yang, Supporting nickel on vanadium nitride for comparable hydrogen evolution performance to platinum in alkaline solution, J. Mater. Chem. A. 9 (2021) 19669–19674, https://doi.org/10.1039/d1ta02760c.

[11] C. Yang, R. Zhao, H. Xiang, J. Wu, W. Zhong, W. Li, Q. Zhang, N. Yang, X. Li, Ni-activated transition metal carbides for efficient hydrogen evolution in acidic and alkaline solutions, Adv. Energy Mater. 10 (2020) 1–10, https://doi.org/10.1002/aenm.202002260.

[12] R. Ding, Y. Chen, X. Li, Z. Rui, K. Hua, Y. Wu, X. Duan, X. Wang, J. Li, J. Liu, Atomically dispersed, low-coordinate Co-N sites on carbon nanotubes as inexpensive and efficient electrocatalysts for hydrogen evolution, Small. 18 (2022) 1–8, https://doi.org/10.1002/smll.202105335.

[13] H. Jin, X. Liu, A. Vasileff, Y. Jiao, Y. Zhao, Y. Zheng, S.Z. Qiao, Single-crystal nitrogen-rich two-dimensional Mo_5N_6 nanosheets for efficient and stable seawater splitting, ACS Nano 12 (2018) 12761–12769, https://doi.org/10.1021/acsnano.8b07841.

[14] B. Liu, B. He, H.-Q. Peng, Y. Zhao, J. Cheng, J. Xia, J. Shen, T.-W. Ng, X. Meng, C.-S. Lee, W. Zhang, Unconventional nickel nitride enriched with nitrogen vacancies as a high-efficiency electrocatalyst for hydrogen evolution, Adv. Sci. 5 (2018), 1800406, https://doi.org/10.1002/advs.201800406.

[15] Z. Chen, Y. Song, J. Cai, X. Zheng, D. Han, Y. Wu, Y. Zang, S. Niu, Y. Liu, J. Zhu, X. Liu, G. Wang, Tailoring the d-band centers enables Co_4N nanosheets to be highly active for hydrogen evolution catalysis, Angew. Chem., Int. Ed. 57 (2018) 5076–5080, https://doi.org/10.1002/anie.201801834.

[16] C. Pi, C. Huang, Y. Yang, H. Song, X. Zhang, Y. Zheng, B. Gao, J. Fu, P.K. Chu, K. Huo, In situ formation of N-doped carbon-coated porous MoP nanowires: A highly efficient electrocatalyst for hydrogen evolution reaction in a wide pH range, Appl. Catal. B Environ. 263 (2020), 118358, https://doi.org/10.1016/j.apcatb.2019.118358.

[17] Y. Pan, Y. Lin, Y. Chen, Y. Liu, C. Liu, Cobalt phosphide-based electrocatalysts: Synthesis and phase catalytic activity comparison for hydrogen evolution, J. Mater. Chem. A. 4 (2016) 4745–4754, https://doi.org/10.1039/c6ta00575f.

[18] C. Huang, J. Zhou, D. Duan, Q. Zhou, J. Wang, B. Peng, L. Yu, Y. Yu, Roles of heteroatoms in electrocatalysts for alkaline water splitting: A review focusing on the reaction mechanism, Chinese J. Catal. 43 (2022) 2091–2110, https://doi.org/10.1016/S1872-2067(21)64052-4.

[19] L. Liao, C. Cheng, H. Zhou, Y. Qi, D. Li, F. Cai, B. Yu, R. Long, F. Yu, Accelerating pH-universal hydrogen-evolving activity of a hierarchical hybrid of cobalt and dinickel phosphides by interfacial chemical bonds, Mater. Today Phys. 22 (2022), 100589, https://doi.org/10.1016/j.mtphys.2021.100589.

[20] J. Li, X. Wang, Y. Wang, Y. Zhao, C. Ma, T. Zhan, L. Chen, C. Zhao, J. Lan, Z. Xiao, P. Wu, Highly-dispersed Ni, N-doped Mo_2C nanoparticles prepared from organic-derived polyoxomolybdates for efficient electrocatalytic hydrogen evolution, Int. J. Hydrogen Energy. 47 (2022) 28915–28923, https://doi.org/10.1016/j.ijhydene.2022.06.241.

[21] X. Yang, J. Cheng, X. Yang, Y. Xu, W. Sun, J. Zhou, Facet-tunable coral-like Mo_2C catalyst for electrocatalytic hydrogen evolution reaction, Chem. Eng. J. 451 (2023), 138977, https://doi.org/10.1016/j.cej.2022.138977.

[22] S. Wu, M. Chen, W. Wang, J. Zhou, X. Tang, D. Zhou, C. Liu, Molybdenum carbide nanoparticles assembling in diverse heteroatoms doped carbon matrix as efficient hydrogen evolution electrocatalysts in acidic and alkaline medium, Carbon N. Y. 171 (2021) 385–394, https://doi.org/10.1016/j.carbon.2020.09.037.

[23] X. Liu, X. Jiang, G. Shao, H. Xiang, Z. Li, Y. Jin, Y. Chen, H. Jiang, H. Li, J. Shui, Y. Feng, S. Liu, Activating the electrocatalysis of MoS_2 basal plane for hydrogen evolution via atomic defect configurations, Small 18 (2022) 1–9, https://doi.org/10.1002/smll.202200601.

[24] S. Geng, F. Tian, M. Li, Y. Liu, J. Sheng, W. Yang, Y. Yu, Y. Hou, Activating interfacial S sites of MoS_2 boosts hydrogen evolution electrocatalysis, Nano Res. 15 (2022) 1809–1816, https://doi.org/10.1007/s12274-021-3755-7.

[25] Y. Ma, D. Leng, X. Zhang, J. Fu, C. Pi, Y. Zheng, B. Gao, X. Li, N. Li, P.K. Chu, Y. Luo, K. Huo, Enhanced activities in alkaline hydrogen and oxygen evolution reactions on MoS_2 electrocatalysts by in-plane sulfur defects coupled with transition metal doping, Small. 18 (2022), 2203173, https://doi.org/10.1002/smll.202203173.

[26] C. Huang, L. Yu, W. Zhang, Q. Xiao, J. Zhou, Y. Zhang, P. An, J. Zhang, Y. Yu, N-doped Ni-Mo based sulfides for high-efficiency and stable hydrogen evolution reaction, Appl. Catal. B Environ. 276 (2020), 119137, https://doi.org/10.1016/j.apcatb.2020.119137.

[27] Y. Zhang, P. Guo, S. Guo, X. Xin, Y. Wang, W. Huang, M. Wang, B. Yang, A. Jorge Sobrido, J.B. Ghasemi, J. Yu, X. Li, Gradient heating epitaxial growth gives well lattice-matched Mo_2C-Mo_2N heterointerfaces that boost both electrocatalytic hydrogen evolution and water vapor splitting, Angew. Chem., Int. Ed. 61 (2022), e202209703, https://doi.org/10.1002/anie.202209703.

[28] L. Wu, F. Zhang, S. Song, M. Ning, Q. Zhu, J. Zhou, G. Gao, Z. Chen, Q. Zhou, X. Xing, T. Tong, Y. Yao, J. Bao, L. Yu, S. Chen, Z. Ren, Efficient alkaline water/seawater hydrogen evolution by a nanorod-nanoparticle-structured Ni-MoN catalyst with fast water-dissociation kinetics, Adv. Mater. 34 (2022) 1–12, https://doi.org/10.1002/adma.202201774.

[29] L. Yu, S. Song, B. McElhenny, F. Ding, D. Luo, Y. Yu, S. Chen, Z. Ren, A universal synthesis strategy to make metal nitride electrocatalysts for hydrogen evolution reaction, J. Mater. Chem. A. 7 (2019) 19728–19732, https://doi.org/10.1039/c9ta05455c.

[30] C. Wang, X. Lv, P. Zhou, X. Liang, Z. Wang, Y. Liu, P. Wang, Z. Zheng, Y. Dai, Y. Li, M.H. Whangbo, B. Huang, Molybdenum nitride electrocatalysts for hydrogen evolution more efficient than platinum/carbon: Mo_2N/CeO_2@nickel foam, ACS Appl. Mater. Interfaces 12 (2020) 29153–29161, https://doi.org/10.1021/acsami.0c02851.

[31] Y. Gong, L. Wang, H. Xiong, M. Shao, L. Xu, A. Xie, S. Zhuang, Y. Tang, X. Yang, Y. Chen, P. Wan, 3D self-supported Ni nanoparticle@N-doped carbon nanotubes anchored on NiMoN pillars for the hydrogen evolution reaction with high activity and anti-oxidation ability, J. Mater. Chem. A 7 (2019) 13671–13678, https://doi.org/10.1039/C9TA03473K.

[32] P. Wang, X. Zhang, J. Zhang, S. Wan, S. Guo, G. Lu, J. Yao, X. Huang, Precise tuning in platinum-nickel/nickel sulfide interface nanowires for synergistic hydrogen evolution catalysis, Nat. Commun. 8 (2017) 1–9, https://doi.org/10.1038/ncomms14580.

[33] L. Dong, G.R. Chang, Y. Feng, X.Z. Yao, X.Y. Yu, Regulating Ni site in NiV LDH for efficient electrocatalytic production of formate and hydrogen by glycerol electrolysis, Rare Met. 41 (2022) 1583–1594, https://doi.org/10.1007/s12598-021-01881-3.

[34] X. Liu, L. Zhang, L. Li, X. Ye, H. Chen, Z. Wei, Mo_2N-Ni/NF heterostructure boosts electrocatalytic hydrogen evolution with Pt-like activity, Inorg. Chem. 59 (2020) 16514–16521, https://doi.org/10.1021/acs.inorgchem.0c02369.

[35] X. Lang, M.A. Qadeer, G. Shen, R. Zhang, S. Yang, J. An, L. Pan, J.J. Zou, A Co-Mo_2N composite on a nitrogen-doped carbon matrix with hydrogen evolution activity comparable to that of Pt/C in alkaline media, J. Mater. Chem. A 7 (2019) 20579–20583, https://doi.org/10.1039/c9ta07749a.

[36] R. Zhang, L. Xu, Z. Wu, L. Wang, J. Zhang, Y. Tang, L. Xu, A. Xie, Y. Chen, H. Zhang, P. Wan, Nitrogen doped carbon encapsulated hierarchical NiMoN as highly active and durable HER electrode for repeated ON/OFF water electrolysis, Chem. Eng. J. 436 (2022), 134931, https://doi.org/10.1016/j.cej.2022.134931.

[37] W. Zhang, Y. Tang, L. Yu, X.Y. Yu, Activating the alkaline hydrogen evolution performance of Mo-incorporated $Ni(OH)_2$ by plasma-induced heterostructure, Appl. Catal. B Environ. 260 (2020), 118154, https://doi.org/10.1016/j.apcatb.2019.118154.

[38] W.F. Chen, K. Sasaki, C. Ma, A.I. Frenkel, N. Marinkovic, J.T. Muckerman, Y. Zhu, R.R. Adzic, Hydrogen-evolution catalysts based on non-noble metal nickel-molybdenum nitride nanosheets, Angew. Chem. 124 (2012) 6235–6239, https://doi.org/10.1002/ange.201200699.

[39] L. Jia, J. Li, X. Yu, L. Feng, L. Yang, Y. Yang, W. Ye, B. Liu, In situ synthesis of nanorod arrays of nickel-molybdenum nitrides as stable electrocatalysts for hydrogen evolution reactions, ACS Appl. Nano Mater. 6 (2023) 1050–1058, https://doi.org/10.1021/acsanm.2c04496.

[40] P. Zhou, X. Lv, D. Xing, F. Ma, Y. Liu, Z. Wang, P. Wang, Z. Zheng, Y. Dai, B. Huang, High-efficient electrocatalytic overall water splitting over vanadium doped hexagonal $Ni_{0.2}Mo_{0.8}N$, Appl. Catal. B Environ. 263 (2020), 118330, https://doi.org/10.1016/j.apcatb.2019.118330.

[41] W. Hua, H. Sun, H. Liu, Y. Li, J.G. Wang, Interface engineered NiMoN/Ni_3N heterostructures for enhanced alkaline hydrogen evolution reaction, Appl. Surf. Sci. 540 (2021), 148407, https://doi.org/10.1016/j.apsusc.2020.148407.

[42] H. Guo, A. Wu, Y. Xie, H. Yan, D. Wang, L. Wang, C. Tian, 2D porous molybdenum nitride/cobalt nitride heterojunction nanosheets with interfacial electron redistribution for effective electrocatalytic overall water splitting, J. Mater. Chem. A. 9 (2021) 8620–8629, https://doi.org/10.1039/d0ta11997k.

[43] B. Wang, L. Guo, J. Zhang, Y. Qiao, M. He, Q. Jiang, Y. Zhao, X. Shi, F. Zhang, Synthesis of nickel nitride-based 1D/0D heterostructure via a morphology-inherited nitridation strategy for efficient electrocatalytic hydrogen evolution, Small. 18 (2022) 1–9, https://doi.org/10.1002/smll.202201927.

[44] C.C.L. McCrory, S. Jung, J.C. Peters, T.F. Jaramillo, Benchmarking heterogeneous electrocatalysts for the oxygen evolution reaction, J. Am. Chem. Soc. 135 (2013) 16977–16987, https://doi.org/10.1021/ja407115p.

[45] G. Kresse, J. Furthmüller, Efficiency of ab-initio total energy calculations for metals and semiconductors using a plane-wave basis set, Comput. Mater. Sci. 6 (1996) 15–50, https://doi.org/10.1016/0927-0256(96)00008-0.

[46] G. Kresse, J. Furthmüller, Efficient iterative schemes for ab initio total-energy calculations using a plane-wave basis set, Phys. Rev. B. 54 (1996) 11169–11186, https://doi.org/10.1103/PhysRevB.54.11169.

[47] J.P. Perdew, K. Burke, M. Ernzerhof, Generalized gradient approximation made simple, Phys. Rev. Lett. 77 (1996) 3865–3868, https://doi.org/10.1103/PhysRevLett.77.3865.

[48] G. Kresse, D. Joubert, From ultrasoft pseudopotentials to the projector augmented-wave method, Phys. Rev. B. 59 (1999) 1758–1775, https://doi.org/10.1103/PhysRevB.59.1758.

[49] P.E. Blöchl, Projector augmented-wave method, Phys. Rev. B. 50 (1994) 17953–17979, https://doi.org/10.1103/PhysRevB.50.17953.

[50] S. Grimme, J. Antony, S. Ehrlich, H. Krieg, A consistent and accurate ab initio parametrization of density functional dispersion correction (DFT-D) for the 94 elements H-Pu, J. Chem. Phys. 132 (15) (2010), 154104, https://doi.org/10.1063/1.3382344.

[51] C. Pi, X. Li, X. Zhang, H. Song, Y. Zheng, B. Gao, A. Kızılaslan, P.K. Chu, K. Huo, In-plane Mott-Schottky effects enabling efficient hydrogen evolution from Mo_5N_6-MoS_2 heterojunction nanosheets in universal-pH electrolytes, Small 18 (2022), 2201137, https://doi.org/10.1002/smll.202201137.

[52] C. Huang, C. Pi, X. Zhang, K. Ding, P. Qin, J. Fu, X. Peng, B. Gao, P.K. Chu, K. Huo, In situ synthesis of MoP nanoflakes intercalated N-doped graphene nanobelts from MoO_3-amine hybrid for high-efficient hydrogen evolution reaction, Small 14 (2018) 1–7, https://doi.org/10.1002/smll.201800667.

[53] Y. Lu, Z. Li, Y. Xu, L. Tang, S. Xu, D. Li, J. Zhu, D. Jiang, Bimetallic Co-Mo nitride nanosheet arrays as high-performance bifunctional electrocatalysts for overall water splitting, Chem. Eng. J. 411 (2021), 128433, https://doi.org/10.1016/j.cej.2021.128433.

[54] Z. Li, A. Wu, Y. Xie, Y. Gu, H. Yan, D. Wang, S. Wang, C. Jin, L. Wang, C. Tian, Integration of heterointerface and porosity engineering to achieve efficient hydrogen evolution of 2D porous NiMoN nanobelts coupled with Ni particles, Electrochim. Acta 403 (2022), 139702, https://doi.org/10.1016/j.electacta.2021.139702.

[55] X. Shi, A. Wu, H. Yan, L. Zhang, C. Tian, L. Wang, H. Fu, A "MOFs plus MOFs" strategy toward Co-Mo_2N tubes for efficient electrocatalytic overall water splitting, J. Mater. Chem. A 6 (2018) 20100–20109, https://doi.org/10.1039/c8ta07906d.

[56] B. Chang, J. Yang, Y. Shao, L. Zhang, W. Fan, B. Huang, Y. Wu, X. Hao, Bimetallic NiMoN nanowires with a preferential reactive facet: An ultraefficient bifunctional electrocatalyst for overall water splitting, ChemSusChem 11 (2018) 3198–3207, https://doi.org/10.1002/cssc.201801337.

[57] F. Liu, Y. Tang, J. Zhao, Y. Bai, J. Chen, L. Tian, S.S.A. Shah, S. juan Bao, Carbon dots-induced carbon-coated Ni and Mo_2N nanosheets for efficient hydrogen production, Electrochim. Acta 424 (2022) 1-7. doi: 10.1016/j.electacta.2022.140671.

[58] H. Song, S. Guo, X. Zhang, Y. Yang, B. Gao, Y. Pi, C. Pi, P.K. Chu, K. Huo, In-Situ and controllable construction of Mo_2N embedded Mo_2C nanobelts as robust electrocatalyst for superior pH-universal hydrogen evolution reaction, J. Alloys Compd. 918 (2022), 165611, https://doi.org/10.1016/j.jallcom.2022.165611.

[59] T. Wang, P. Wang, W. Zang, X. Li, D. Chen, Z. Kou, S. Mu, J. Wang, Nanoframes of Co_3O_4-Mo_2N heterointerfaces enable high-performance bifunctionality toward both electrocatalytic HER and OER, Adv. Funct. Mater. 32 (2022), 2107382, https://doi.org/10.1002/adfm.202107382.

[60] R. Cheng, H. He, Z. Pu, I.S. Amiinu, L. Chen, Z. Wang, G. Li, S. Mu, Shrunken hollow Mo-N/Mo-C nanosphere structure for efficient hydrogen evolution in a broad pH range, Electrochim. Acta 298 (2019) 799–805, https://doi.org/10.1016/j.electacta.2018.12.128.

[61] W. Wang, L. Yang, J. Chen, S. Wu, M. Chen, X. Liang, D. Zhou, C. Liu, Realizing electronic modulation on Mo sites for efficient hydrogen evolution reaction, J. Mater. Chem. A 8 (2020) 18180–18187, https://doi.org/10.1039/d0ta05957a.

[62] H. Prats, K. Chan, The determination of the HOR/HER reaction mechanism from experimental kinetic data, Phys. Chem. Chem. Phys. 23 (2021) 27150–27158, https://doi.org/10.1039/D1CP04134G.

[63] W. Peng, Z. Wang, R. Lu, Q. Li, Z. Wang, Y. Zhao, L. Xu, L. Mai, Artificial heterointerfaces of defect-rich Ni and amorphous/crystalline MoN enable efficient hydrogen evolution reaction, Chem. Eng. J. 457 (2023), 141173, https://doi.org/10.1016/j.cej.2022.141173.

[64] R. Dai, H. Zhang, W. Zhou, Y. Zhou, Z. Ni, J. Chen, S. Zhao, Y. Zhao, F. Yu, A. Chen, R. Wang, T. Sun, Interface engineering of bimetallic nitrides nanowires as a highly efficient bifunctional electrocatalyst for water splitting, J. Alloys Compd. 919 (2022), 165862, https://doi.org/10.1016/j.jallcom.2022.165862.

[65] Q. Liang, L. Zhong, C. Du, Y. Luo, J. Zhao, Y. Zheng, J. Xu, J. Ma, C. Liu, S. Li, Q. Yan, Interfacing epitaxial dinickel phosphide to 2D nickel thiophosphate nanosheets for boosting electrocatalytic water splitting, ACS Nano. 13 (2019) 7975–7984, https://doi.org/10.1021/acsnano.9b02510.

[66] Y. Wen, J. Qi, P. Wei, X. Kang, X. Li, Design of Ni_3N/Co_2N heterojunctions for boosting electrocatalytic alkaline overall water splitting, J. Mater. Chem. A. 9 (2021) 10260–10269, https://doi.org/10.1039/d1ta00885d.

[67] X. Wang, Y. Zheng, W. Sheng, Z.J. Xu, M. Jaroniec, S.Z. Qiao, Strategies for design of electrocatalysts for hydrogen evolution under alkaline conditions, Mater. Today. 36 (2020) 125–138, https://doi.org/10.1016/j.mattod.2019.12.003.

[68] Y. Sun, L. Wang, O. Guselnikova, O. Semyonov, J. Fraser, Y. Zhou, N. López, A. Y. Ganin, Revealing the activity of Co_3Mo_3N and $Co_3Mo_3N_{0.5}$ as electrocatalysts for the hydrogen evolution reaction, J. Mater. Chem. A. 10 (2022) 855–861, https://doi.org/10.1039/d1ta08389a.

[69] A. Badreldin, A. Nabeeh, Z.K. Ghouri, J. Abed, N. Wang, Y. Wubulikasimu, K. Youssef, D. Kumar, M.K. Stodolny, K. Elsaid, E.H. Sargent, A. Abdel-Wahab, Early transition-metal-based binary oxide/nitride for efficient electrocatalytic hydrogen evolution from saline water in different pH environments, ACS Appl. Mater. Interfaces. 13 (2021) 53702–53716, https://doi.org/10.1021/acsami.1c13002.

Supporting Information for

Heterojunction Mo-based Binary and Ternary Nitride Catalysts with Pt-Like Activity for the Hydrogen Evolution Reaction

Xueling Wang[a], Xuming Zhang[a], Yifan Xu[a], Hao Song[a], Xingrui Mi [a], Zihuan Tang[a], Chaoran Pi[a], Jianping Li[a], Biao Gao[a], Yang Zheng[a], Xiang Peng[c], Paul K. Chu[d], Kaifu Huo[b]**

Calculation of turnover frequency (TOF)

The turnover frequency can be calculated by the following formula:

$$TOF = \frac{\text{no. of total hydrogen turnovers/ cm}^2\text{ of geometric area}}{\text{no. of active sites/ cm}^2\text{ of geometric area}}$$ the molecules can be represented as $(j\ \frac{mA}{cm^2}(($ $\frac{1\ C\ s^{-1}}{1000\ mA}(($ $\frac{1\ mol\ of\ e^-}{96485.3\ C}(($ $\frac{1\ mol\ of\ H_2}{2\ mol\ of\ e^-}(($ $\frac{6.022\times10^{23}\cdot H_2\ molecules}{1\ mol\ of\ H_2}($ $=$ $(3.12\times10^{15}\ \frac{H_2\cdot s^{-1}}{cm^2}\ per\ \frac{mA}{cm^2}(\times|j|$ the denominators can be represented as (active sites per real surface area(× A_{ECSA}. Therefore $TOF = \frac{(3.12\times10^{15}\ \frac{H_2\cdot s^{-1}}{cm^2}\ per\ \frac{mA}{cm^2}(\times|j|}{(\text{active sites per real surface area})\times A_{ECSA}}$.

For Mo_2N

$$\text{active sites} = (\frac{6\ \text{atoms/ unit cell}}{72.15\ Å^3\text{/ unit cell}}(^{\frac{2}{3}} = 1.91\times10^{15}\ \text{atoms cm}^{-2}_{real}$$

$$A^{Mo_2N}_{ECSA} = \frac{95.01\times10^3\ \mu F\ cm^{-2}}{60\ \mu F\ cm^{-2}\ per\ cm^2_{ECSA}} = 1583.5\ cm^2_{ECSA}$$

For $Ni_{0.2}Mo_{0.8}N$

$$\text{active sites} = (\frac{2\ \text{atoms/ unit cell}}{19.42\ Å3\text{/ unit cell}}(^{\frac{2}{3}} = 2.20\times10^{15}\ \text{atoms cm}^{-2}_{real}$$

$$A^{Ni_{0.2}Mo_{0.8}N}_{ECSA} = \frac{109.19\times10^3\ \mu F\ cm^{-2}}{60\ \mu F\ cm^{-2}\ per\ cm^2_{ECSA}} = 1819.8\ cm^2_{ECSA}$$

For $Mo_2N/Ni_{0.2}Mo_{0.8}N$

The number of active sites was reckoned with the relative content of each phase derived from the stoichiometric ratio.

$$\text{active sites}=0.45\times1.91\times10^{15}+0.55\times2.20\times10^{15} = 2.07\times10^{15}\ \text{atoms cm}^{-2}_{real}$$

$$A^{Mo_2N/Ni_{0.2}Mo_{0.8}N}_{ECSA} = \frac{175.14\times10^3\ \mu F\ cm^{-2}}{60\ \mu F\ cm^{-2}\ per\ cm^2_{ECSA}} = 2919\ cm^2_{ECSA}$$

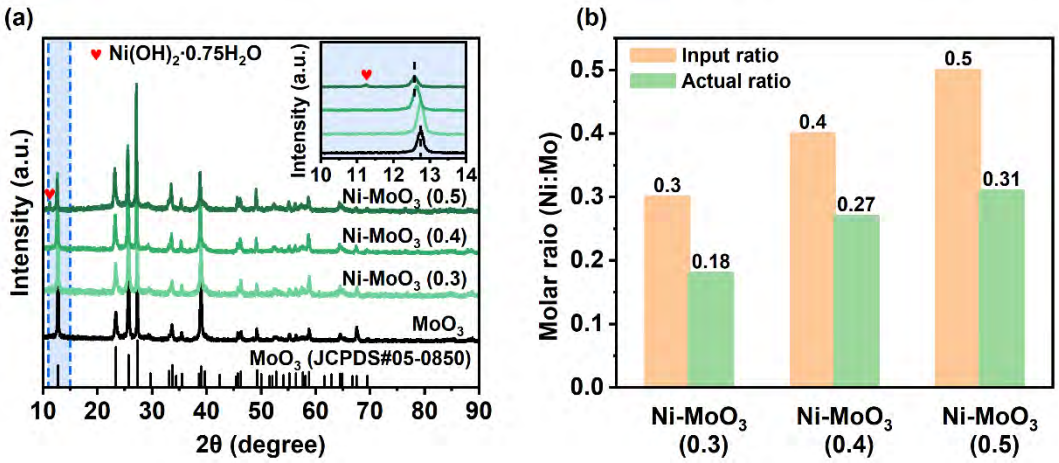

Figure S1. (a(XRD patterns of Ni^{2+} intercalated layered MoO_3 samples (b(ICP-MS results of the Ni^{2+} intercalated layered MoO_3 samples with different input Ni/Mo mole ratios.

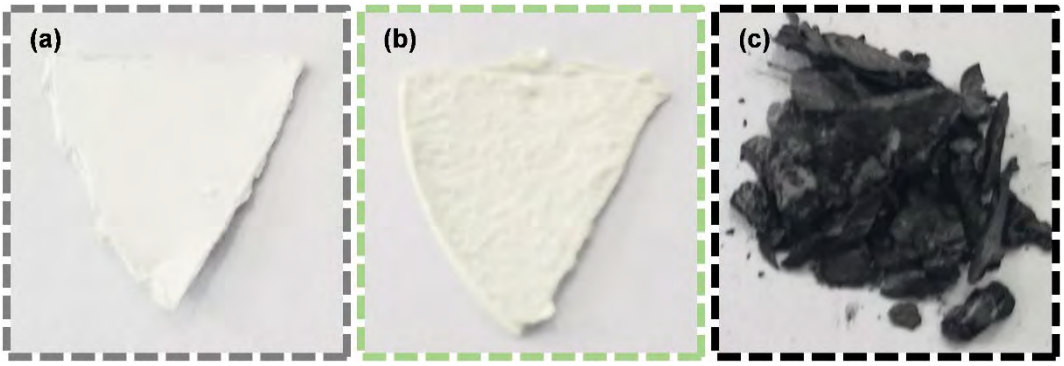

Figure S2. Photos of (a(MoO_3 (b(Ni-MoO_3 (0.4((c($Mo_2N/Ni_{0.2}Mo_{0.8}N$-2 samples.

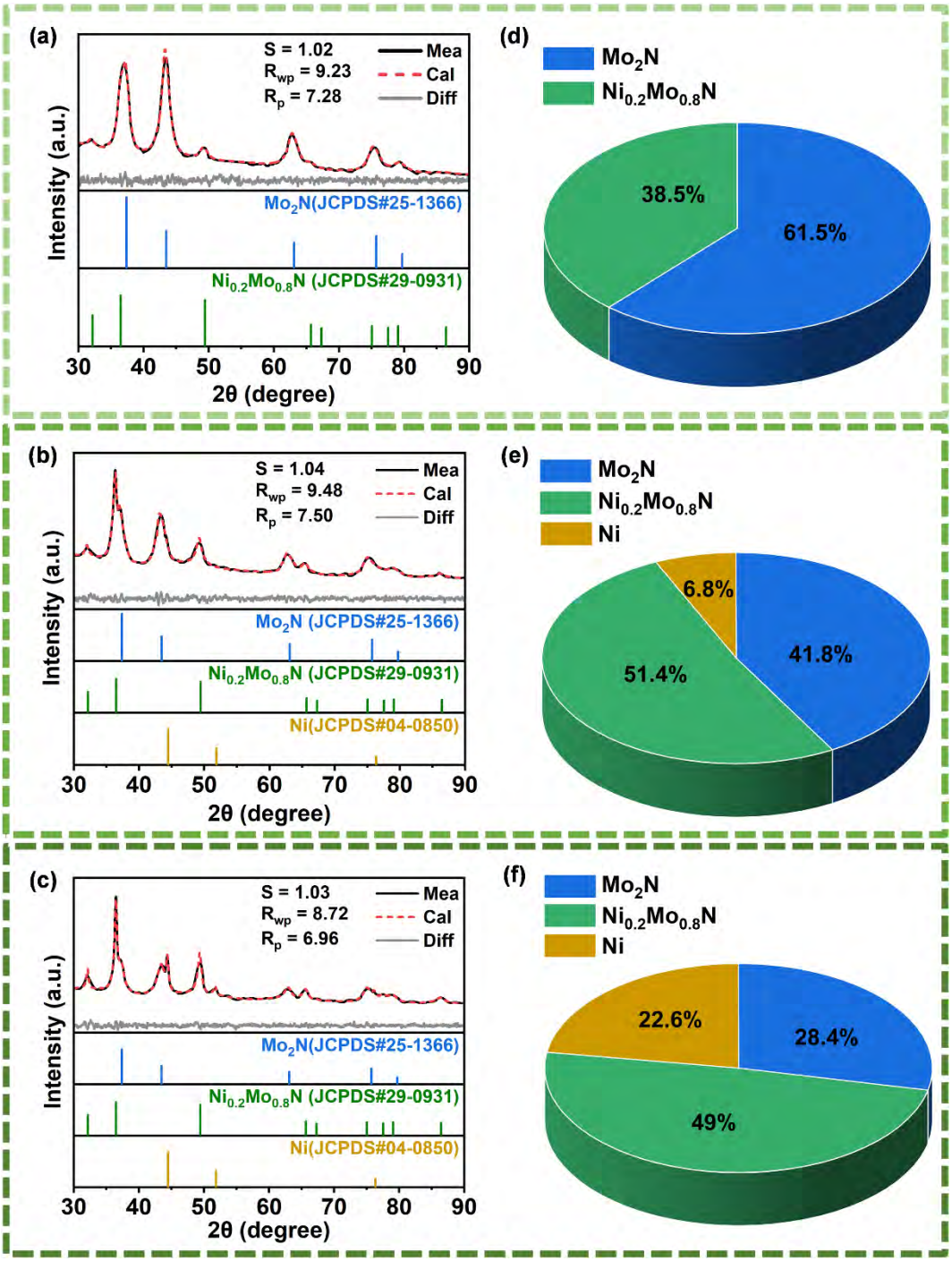

Figure S3. XRD patterns of (a($Mo_2N/Ni_{0.2}Mo_{0.8}N$-1 (b($Mo_2N/Ni_{0.2}Mo_{0.8}N$-2 (c($Mo_2N/Ni_{0.2}Mo_{0.8}N$-3 and their corresponding composition ratio refined by Rietveld method.

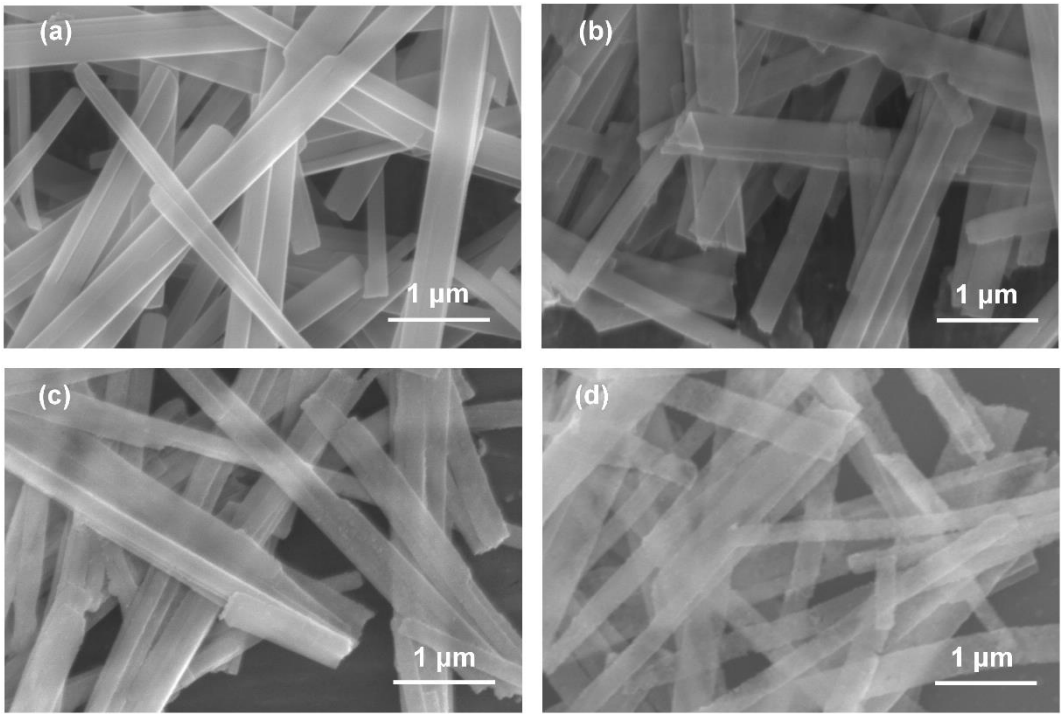

Figure S4. SEM images of (a(MoO_3 (b(Ni-MoO_3 (0.3((c(Ni-MoO_3 (0.4(and (d(Ni-MoO_3 (0.5(.

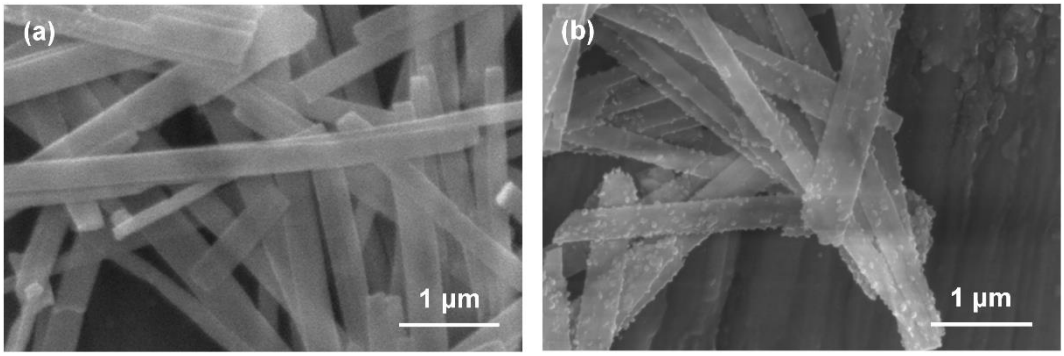

Figure S5. SEM images of (a($Mo_2N/Ni_{0.2}Mo_{0.8}N$-1 and (b($Mo_2N/Ni_{0.2}Mo_{0.8}N$-3.

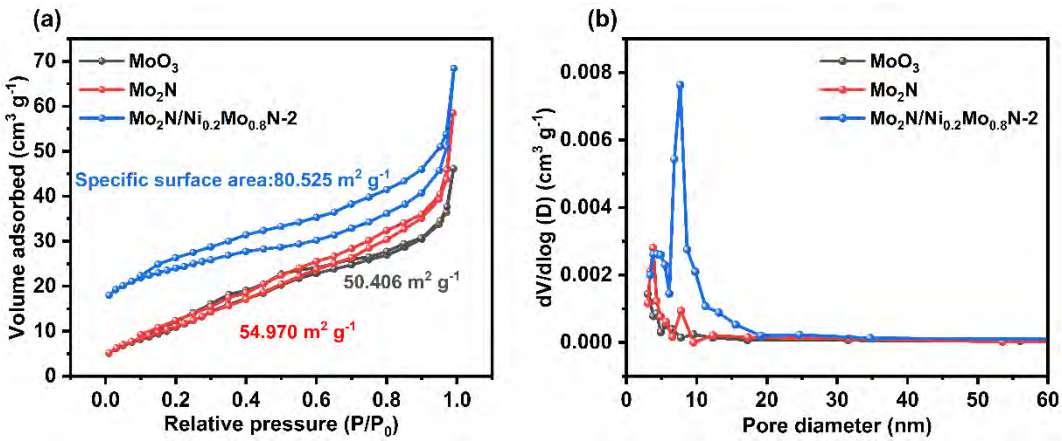

Figure S6. (a(N_2 adsorption/desorption isotherms and (b(the pore size distribution of MoO_3 Mo_2N and $Mo_2N/Ni_{0.2}Mo_{0.8}N$-2 NBs.

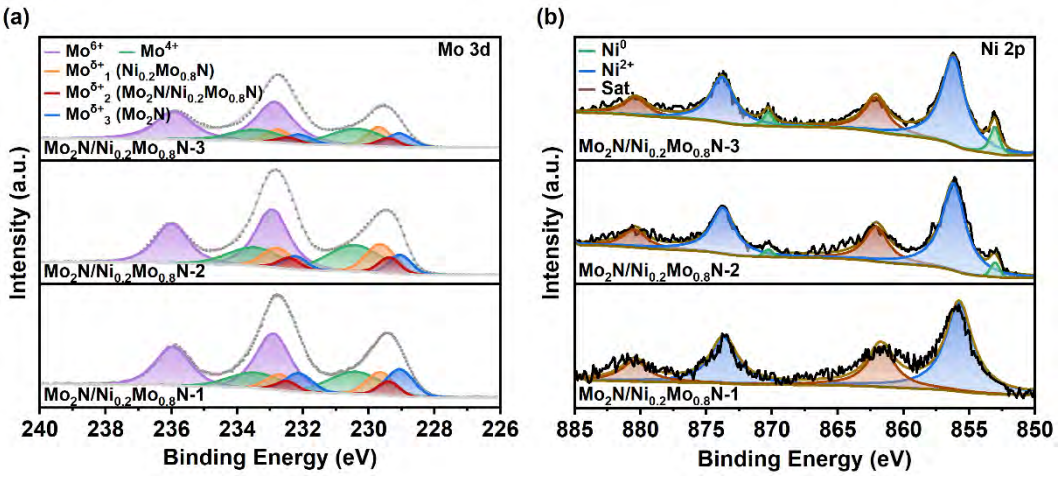

Figure S7. The high resolution XPS spectra of (a(Mo 3*d* and (b(Ni 2*p* of $Mo_2N/Ni_{0.2}Mo_{0.8}N$.

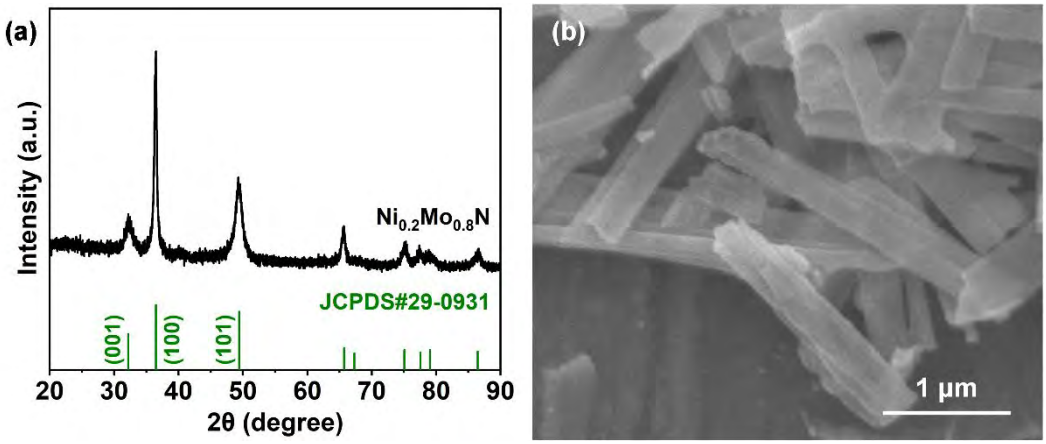

Figure S8. (a(XRD pattern and (b(SEM image of $Ni_{0.2}Mo_{0.8}N$ NBs after acid pickling nitrided Ni-MoO_3 (1.0(sample.

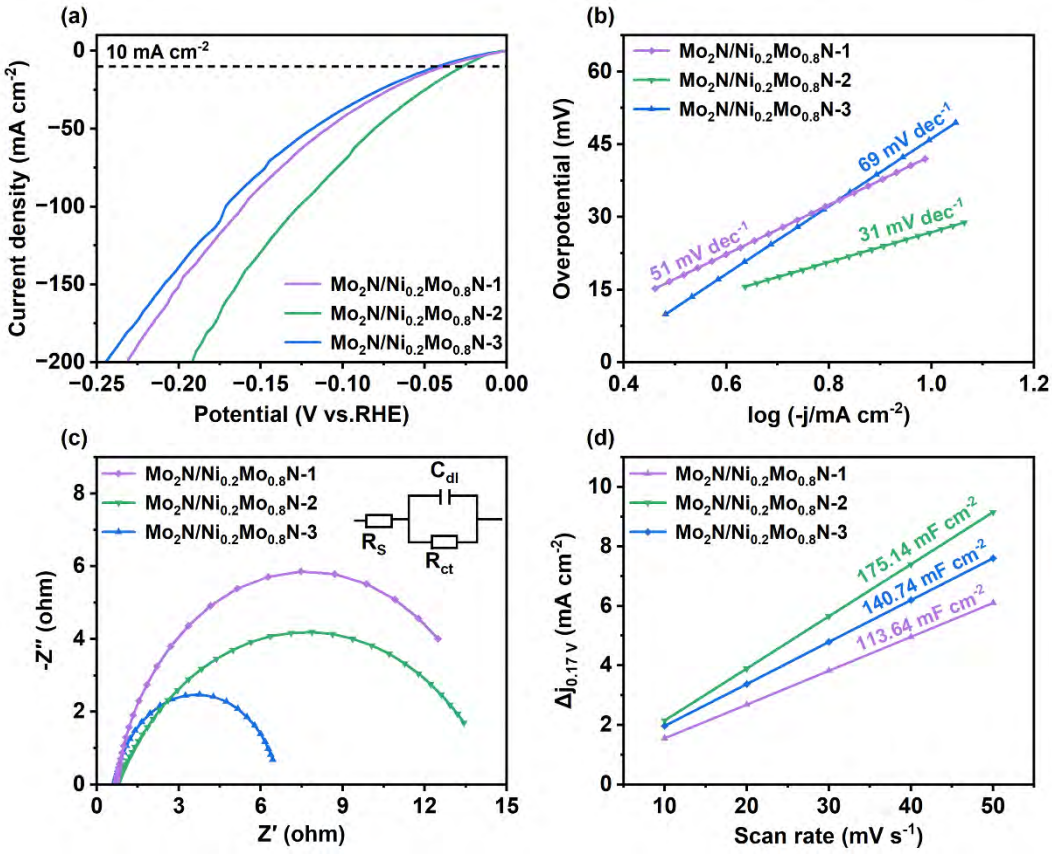

Figure S9. (a(LSV curves (b(Tafel slopes (c(Nyquist plots and (d(Double-layer capacitance (C_{dl}(of $Mo_2N/Ni_{0.2}Mo_{0.8}N$.

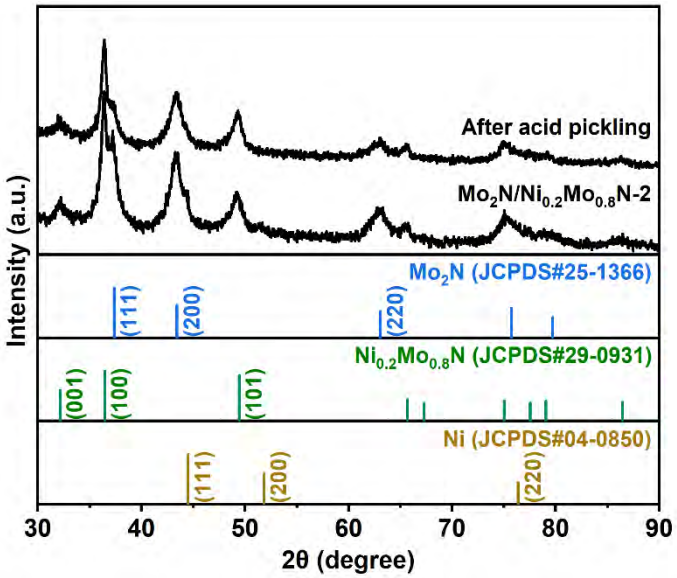

Figure S10. XRD patterns of $Mo_2N/Ni_{0.2}Mo_{0.8}N$-2 before and after acid pickling in 0.05 M HCl for 3 h at room temperature.

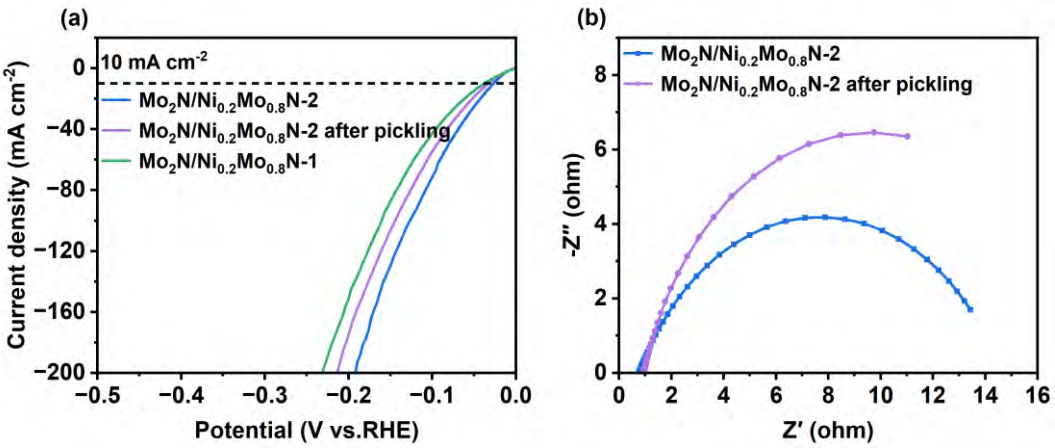

Figure S11. (a(LSV curves and (b(Nyquist plots of $Mo_2N/Ni_{0.2}Mo_{0.8}N$-2 before and after acid pickling.

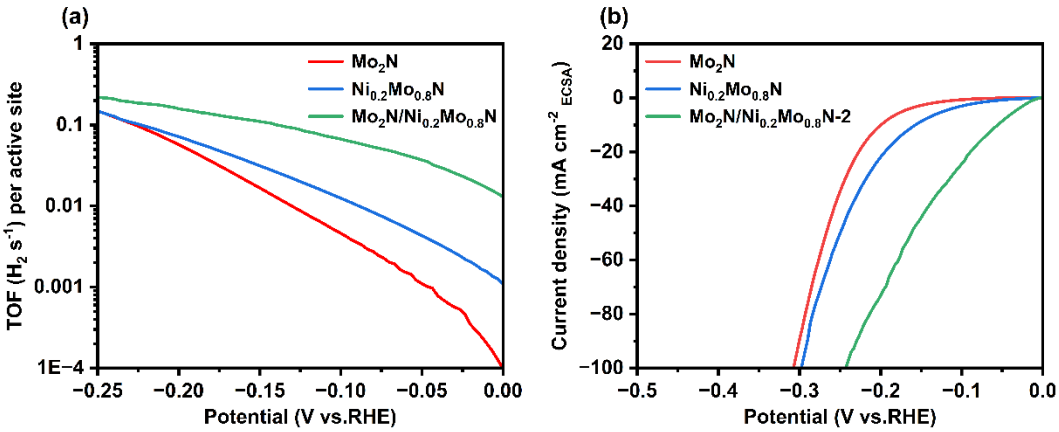

Figure S12. (a(TOF values and (b(ECSA-normalized polarization curves of the Mo_2N $Ni_{0.2}Mo_{0.8}N$ and $Mo_2N/Ni_{0.2}Mo_{0.8}N$-2 catalysts.

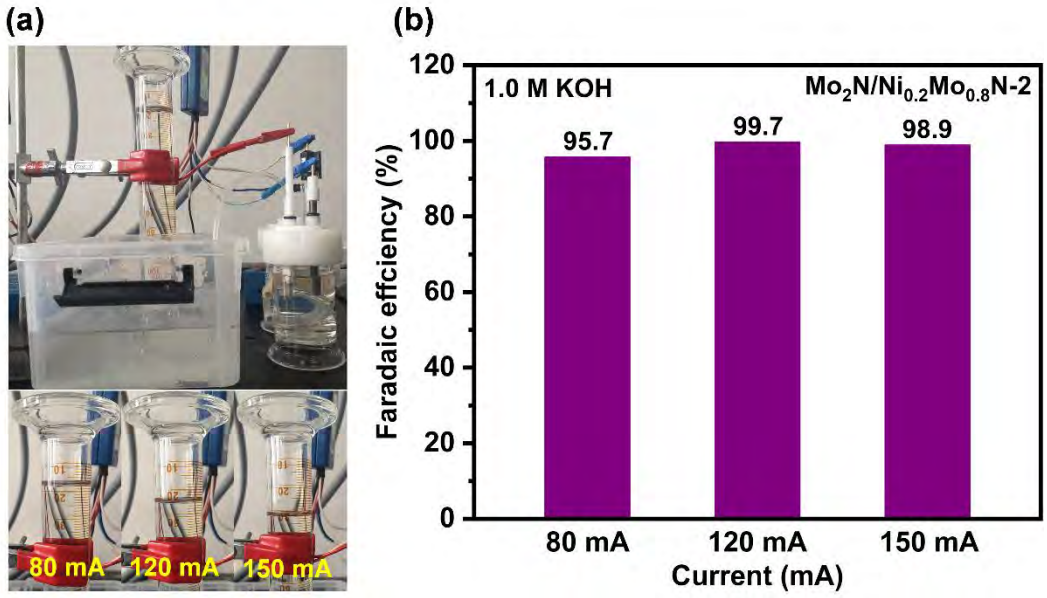

Figure S13. (a(Digital photograph of H_2 gas collection in three-electrode system (b(The faradic efficiency of HER process calculated at different current for 30 min in three-electrode system.

The FE is calculated by the following formula: $FE = \frac{\frac{m}{22.4}\times n\times F}{I\times t} \times 100\%$ where the m n F I and t stand for volume (0.016 L 0.025 L and 0.031 L(charge transfer number for the formation of one H_2 molecular (n = 2(faradic constant (96485 C(applied current (0.08A 0.12A 0.15A(and duration time (1800 s(.

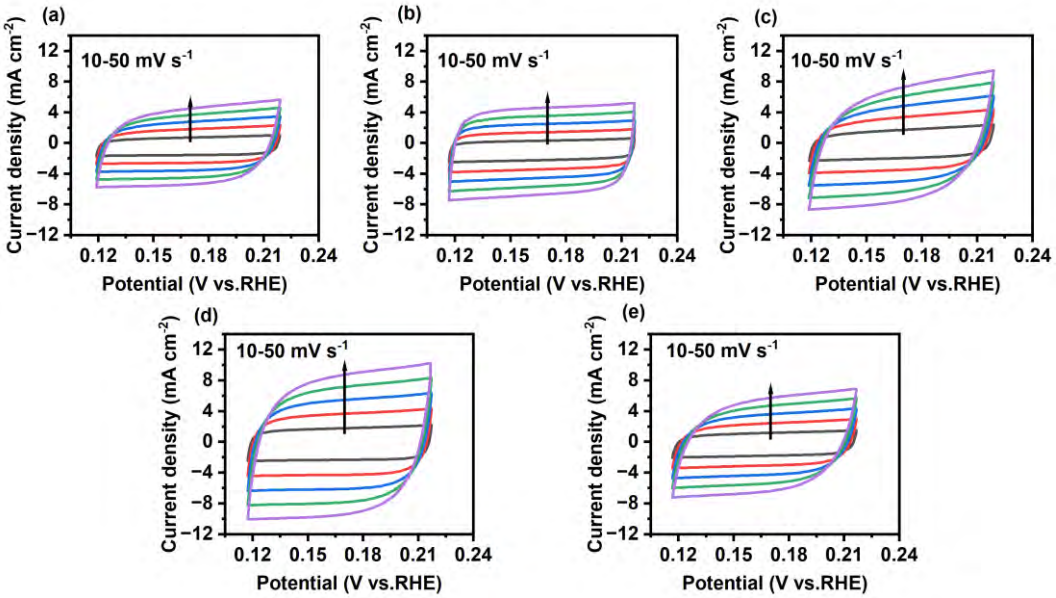

Figure S14. CV curves of (a(Mo_2N (b($Ni_{0.2}Mo_{0.8}N$ (c($Mo_2N/Ni_{0.2}Mo_{0.8}N$-1 (d($Mo_2N/Ni_{0.2}Mo_{0.8}N$-2 and (e($Mo_2N/Ni_{0.2}Mo_{0.8}N$-3 at different scanning rates.

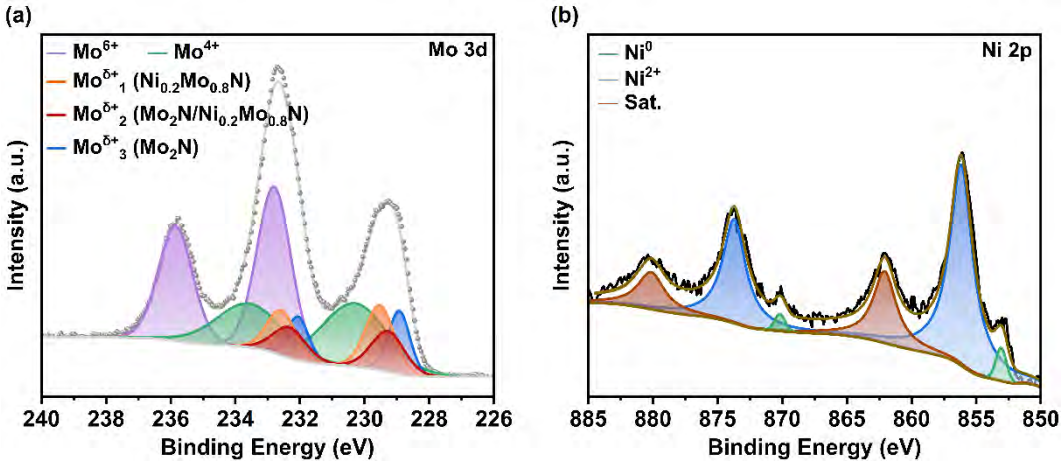

Figure S15. High resolution XPS spectra of (a(Mo 3*d* and (b(Ni 2p of $Mo_2N/Ni_{0.2}Mo_{0.8}N$-2 after 2 000 cycles at a scanning rate of 50 mV s^{-1}.

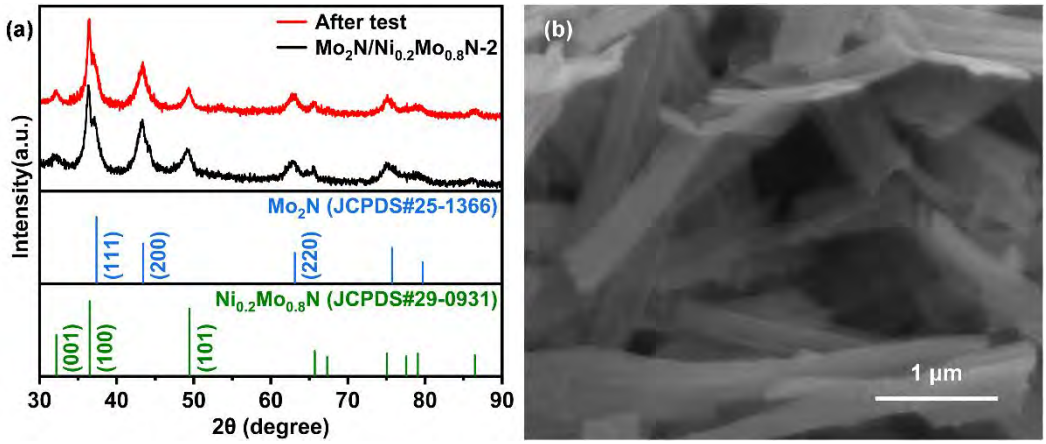

Figure S16. (a(XRD patterns and (b(SEM image of $Mo_2N/Ni_{0.2}Mo_{0.8}N$-2 after chronoamperometric test at a constant overpotential of 80 mV for 90 h.

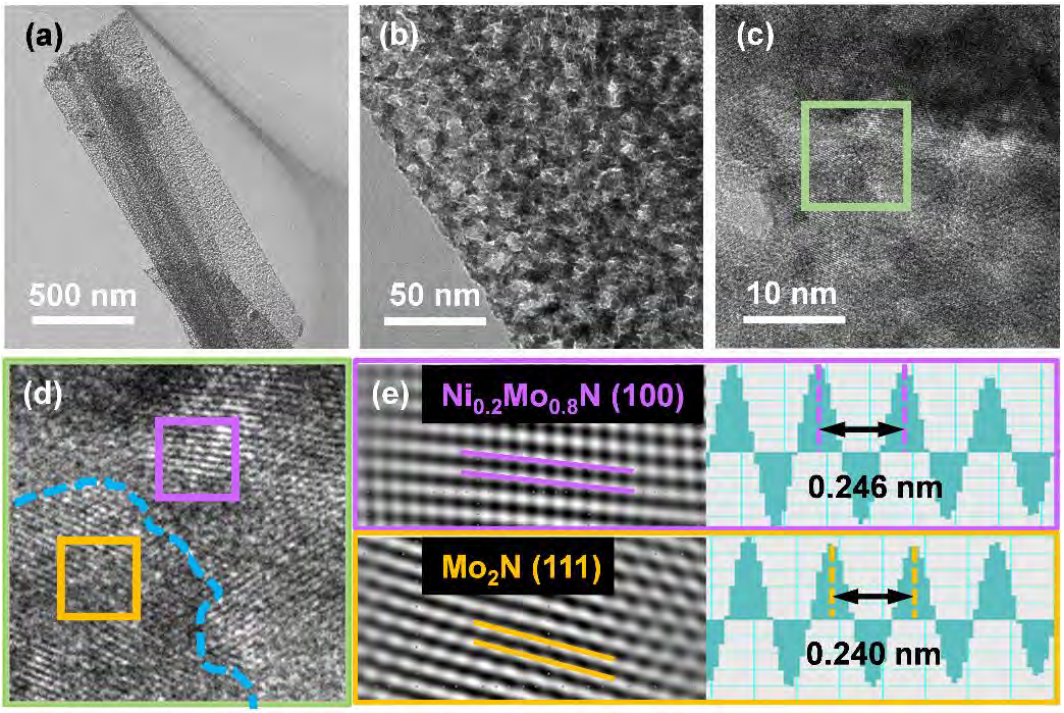

Figure S17. (a(TEM image (b-d(HR-TEM images and (e(Inverse FFT lattice images and interplanar spacing profiles of $Mo_2N/Ni_{0.2}Mo_{0.8}N$-2 after chronoamperometric test at a constant overpotential of 80 mV for 90 h.

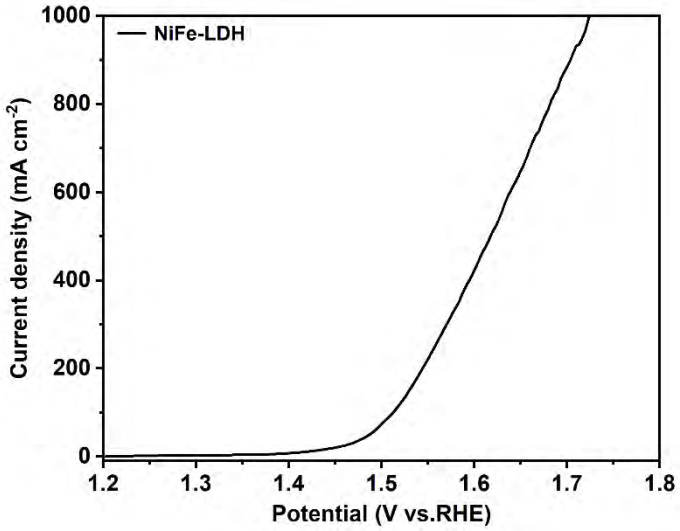

Figure S18. LSV curve of NiFe-LDH on Ni foam.

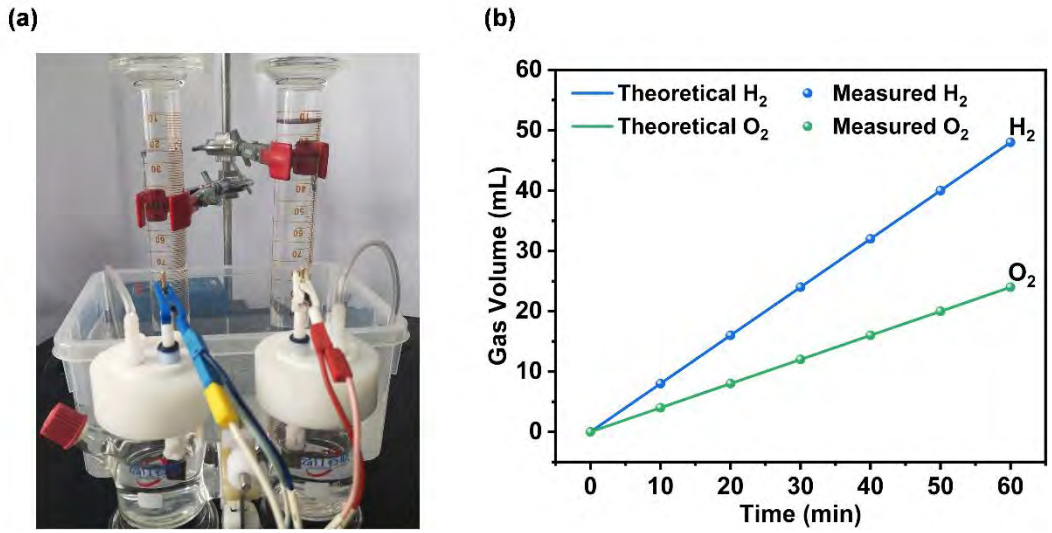

Figure S19. (a(Digital photograph of H_2 and O_2 gas collection in two-electrode system (b(gas yield-time relationship at a constant current of 200 mA for 60 min.

The FE is calculated by the following formula: $FE = \frac{\frac{m}{22.4}\times n\times F}{I\times t} \times 100\%$ where the m n F I and t stand for volume (0.048 L(charge transfer number of H_2 molecular (n = 2(faradic constant (96485 C(applied current (0.20 A(and duration time (3600 s(.

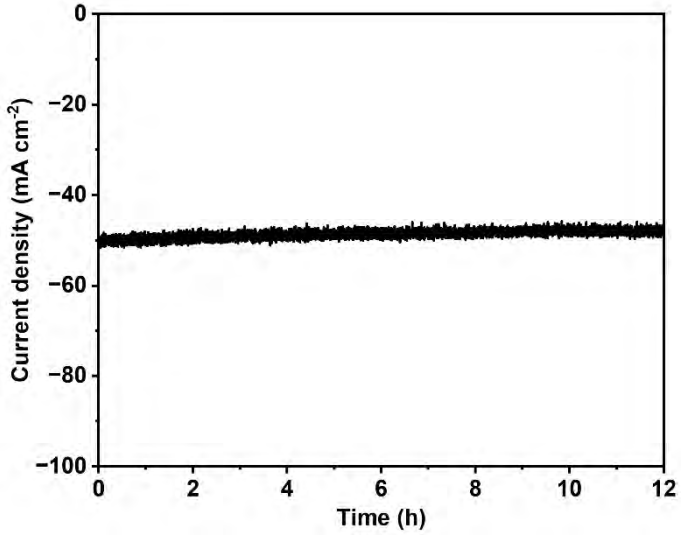

Figure S20. Long-term stability test of the $Mo_2N/Ni_{0.2}Mo_{0.8}N$-2 at a constant overpotential of 80 mV for 12 h in simulated seawater (1.0 M KOH+0.5 M NaCl(.

Table S1 Comparison of $Mo_2N/Ni_{0.2}Mo_{0.8}N$-2 and other reported catalysts in 1.0 M KOH

Catalyst	η_{10} (mA)	η_{100} (mA)	Tafel slope (mV dec^{-1})	Stability (mA cm^{-2} for h)	Reference
$Mo_2N/Ni_{0.2}Mo_{0.8}N$-2	**26**	**127**	**31**	**50 mA cm^{-2} for 30 h**	**This work**
Co-Mo_2N@NC	47	170	43	10 mA cm^{-2} for 12 h	[1]
Mo_2N-Co_xN	29	159	81	10 mA cm^{-2} for 48 h	[2]
NiMoN	109	167	95	10/30/50 mA cm^{-2} for 12 h	[3]
$CoMoN_x$/NF	91	208	70.3	10 mA cm^{-2} for 100 h	[4]
MoN-Co_2N	105	204	82.1	100 mA cm^{-2} for 62 h	[5]
Ni/MoN	24	61	35.5	100 mA cm^{-2} for 200 h	[6]
Mo_2N	73.13	248	66.52	10 mA cm^{-2} for 20 h	[7]
Co-NiMoN	45	148	54.7	25 mA cm^{-2} for 22 h	[8]
Ni_2Mo_3N	21.3	123.8	62	10 mA cm^{-2} for 24 h	[9]
NC/Ni-Mo-N/NF	72	97	94	10 mA cm^{-2} for 12 h	[10]
Ni_3N-Mo_2N/NF	66	160	67.4	20 mA cm^{-2} for 48 h	[11]
Ni_{foam}@Ni-$Ni_{0.2}Mo_{0.8}N$	15	\	39	10 mA cm^{-2} for 110 h	[12]
NiMoN/NiN	49	136	63	20 mA cm^{-2} for 60 h	[13]
Ni/$Ni_{0.2}Mo_{0.8}N$-30	48	207	75	10 mA cm^{-2} for 48 h	[14]
NiMoN-650	50	245	80	10 mA cm^{-2} for 10 h	[15]
Mo_2N@NC	85	\	54	10 mA cm^{-2} for 10 h	[16]
Mo_2N-Ni/NF	20	98	39.9	50 mV cm^{-2} for 100 h	[17]
Ni@NCNT/NiMoN/NF	15	112.5	68	100 mA cm^{-2} for 24 h	[18]
$NiCo_2N$	48	149	78.7	50 mA cm^{-2} for 48 h	[19]
Ni-Mo-N/NG	46.6	159.8	45	10 mA cm^{-2} for 34 h	[20]

References

[1] X. Lang, M. A. Qadeer, G. Shen, R. Zhang, S. Yang, J. An, L. Pan, J.-J. Zou, *J. Mater. Chem. A* **2019**, *7*, 20579.

[2] H. Guo, A. Wu, Y. Xie, H. Yan, D. Wang, L. Wang, C. Tian, *J. Mater. Chem. A* **2021**, *9*, 8620.

[3] Y. Zhang, B. Ouyang, J. Xu, S. Chen, R. S. Rawat, H. J. Fan, *Adv. Energy Mater.* **2016**, *6*, 1600221.

[4] Y. Lu, Z. Li, Y. Xu, L. Tang, S. Xu, D. Li, J. Zhu, D. Jiang, *Chem. Eng. J.* **2021**, *411*, 128433.

[5] X. Wang, X. Han, R. Du, C. Xing, X. Qi, Z. Liang, P. Guardia, J. Arbiol, A. Cabot, J. Li, *ACS Appl. Mater. Interfaces* **2022**, *14*, 41924.

[6] L. Wu, F. Zhang, S. Song, M. Ning, Q. Zhu, J. Zhou, G. Gao, Z. Chen, Q. Zhou, X. Xing, T. Tong, Y. Yao, J. Bao, L. Yu, S. Chen, Z. Ren, *Adv. Mater.* **2022**, *34*, 2201774.

[7] S. Yunqi, L. Jiaming, L. Guoming, X. Kui, *Int. J. Hydrogen Energy* **2021**, *46*, 21777.

[8] Z. Yin, Y. Sun, Y. Jiang, F. Yan, C. Zhu, Y. Chen, *ACS Appl. Mater. Interfaces* **2019**, *11*, 27751.

[9] S. H. Park, T. H. Jo, M. H. Lee, K. Kawashima, C. B. Mullins, H.-K. Lim, D. H. Youn, *J. Mater. Chem. A* **2021**, *9*, 4945.

[10] Y. Xu, M. Liu, S. Wang, K. Ren, M. Wang, Z. Wang, X. Li, L. Wang, H. Wang, *Appl. Catal. B Environ.* **2021**, *298*, 120493.

[11] R. Dai, H. Zhang, W. Zhou, Y. Zhou, Z. Ni, J. Chen, S. Zhao, Y. Zhao, F. Yu, A. Chen, R. Wang, T. Sun, *J. Alloys Compd.* **2022**, *919*, 165862.

[12] J. Jia, M. Zhai, J. Lv, B. Zhao, H. Du, J. Zhu, *ACS Appl. Mater. Interfaces* **2018**, *10*, 30400.

[13] B. Wang, L. Guo, J. Zhang, Y. Qiao, M. He, Q. Jiang, Y. Zhao, X. Shi, F. Zhang, *Small* **2022**, *18*, 2201927.

[14] Z. Li, A. Wu, Y. Xie, Y. Gu, H. Yan, D. Wang, S. Wang, C. Jin, L. Wang, C. Tian, *Electrochim. Acta* **2022**, *403*, 139702.

[15] Z. Yin, Y. Sun, C. Zhu, C. Li, X. Zhang, Y. Chen, *J. Mater. Chem. A* **2017**, *5*, 13648.

[16] Z. Lv, M. Tahir, X. Lang, G. Yuan, L. Pan, X. Zhang, J.-J. Zou, *J. Mater. Chem. A* **2017**, *5*, 20932.

[17] W.-J. Wei, Y. Mu, L. Wei, J.-X. Hu, G.-M. Wang, *Inorg. Chem.* **2021**, *60*, 108.

[18] Y. Gong, L. Wang, H. Xiong, M. Shao, L. Xu, A. Xie, S. Zhuang, Y. Tang, X. Yang, Y. Chen, P. Wan, *J. Mater. Chem. A* **2019**, *7*, 13671.

[19] L. Yu, S. Song, B. McElhenny, F. Ding, D. Luo, Y. Yu, S. Chen, Z. Ren, *J. Mater. Chem. A* **2019**, *7*, 19728.

[20] S. Xue, W. Zhang, Q. Zhang, J. Du, H.-M. Cheng, W. Ren, *Carbon N. Y.* **2020**, *165*, 122.